UNIVERSITÀ DEGLI STUDI DI PADOVA

Dipartimento di Fisica e Astronomia "Galileo Galilei"

Master Degree in Physics

Final Dissertation

The third dredge up in low- and intermediate-mass stars: sensitivity to mixing treatments and evolutionary effects.

Thesis supervisor

Prof. Paola Marigo

Candidate

Francesco Addari

Academic Year 2019/2020

Abstract

The thesis deals with the advanced evolution of low- and intermediate-mass stars ($M_i \lesssim 8M_\odot$), with particular focus on the TP-AGB phase, when thermal pulses periodically take place in the interiors while strong stellar winds progressively erode the external mantle. This study, based on the `MESA` stellar evolution code, aims to investigate the effects of the third dredge-up on the surface properties, i.e. chemical composition, effective temperature, and opacity. Different overshooting schemes and mass loss prescriptions were explored. At the same time, I tested the performance and characteristics of the code, a preliminary but necessary step for possible future developments of the research.

Contents

List of Figures

List of Tables

Introduction

The occurrence of the third dredge-up during the thermally pulsing asymptotic giant branch has critical consequences on both evolution and structure of low- and intermediate-mass stars. The mass range of interest is roughly $0.8M_{\odot} \lesssim M_i \lesssim 8M_{\odot}$, which can be divided in the two classes just mentioned. In this thesis we classify as low-mass stars those which develop a degenerate helium core after the main sequence. The ignition of helium is unstable and trigger a thermonuclear runaway called He-flash. They cover the mass range up to $M_i \simeq 2M_{\odot}$ (for now). Sooner or later all star from both classes reach the TP-AGB phase. These are very luminous and cool stars, peaking their emission at near-infrared wavelengths. They are surrounded by a cold atmosphere, where the gas condensate into dust grains; the composition of the dust dramatically depends on the proprieties of the third dredge-up.

TP-AGB stars are of paramount importance in several fields of modern astrophysics, from spectral energy distribution of galaxies (Bruzual, 2007; Villaume et al., 2015), dust production and chemical enrichment of galaxies (Zhukovska & Henning, 2013; Zhukovska et al., 2016) at both low and high redshift, up to possibly explain multiple stellar populations in globular clusters (Ventura et al., 2016; Slemer et al., 2017). Nevertheless the modeling of this type of stars is still plagued by uncertainties of both numeric and physics nature. The third dredge-up is tightly connected to other processes occurring in this phase, e.g. hot bottom burning, mass loss mechanism. This results in a large heterogeneity among the models of AGB stars in the literature.

The purpose of this thesis is to investigate the effects of the third dredge-up on the surface properties, star evolution and its sensitivity to overshoot mixing and mass loss prescription. To do so, I have learnt and used `MESA` stellar evolution code. That is of course necessary in order to produce accurate TP-AGB models: one has to choose appropriate timestep and meshing schemes alongside reasonable input physics. In addition I implemented and tested a different mass loss routine, which takes into account the carbon-to-oxygen excess (Mattsson et al., 2010; Eriksson et al., 2014; Bladh et al., 2019); that excess may be naturally developed due to the occurrence of third dredge-up. At the same time I tested the performance and characteristics of the code, which is a preliminary but fundamental step for possible future developments of the research.

The thesis is structured in four chapters:

Chapter 1: The first chapter briefly recalls the evolution of low- and intermediate-mass stars, from the pre-main sequence to the white dwarf phase.

Chapter 2: The second chapter describes the code features, the various timestep and meshing schemes and the input physics used to calculate the tracks. The last section is dedicated to the calibration of a solar model, which is a customary procedure to set the value of some free parameters.

Chapter 3: The third chapter contains a discussion on the first two dredge-up episodes, which modifies the surface abundance before the TP-AGB phase.

Chapter 4: The fourth and final chapter constitute the main matter of the thesis. Here I firstly give further evolutionary details of the TP-AGB phase, showing the results of `MESA` calculations of a prototype model. Then I present the results of the investigation about different values of overshooting efficiency in the boundaries of the pulse driven convective zone. After that the discussion passes on the full grid of models comparing the no-overshooting case and the most promising value of $f_{\rm ov,pdcz}$ for different initial masses. In the end I discuss the results found after implementing a carbon-to-oxygen excess mass loss routine inside `MESA`.

Name	Description	First Appearance	Name	Description	First Appearance
PMS	Pre-Main Sequence	Chap. 1	FDUP	First Dredge-UP	Sect. 3.1
ZAMS	Zero-Age Main Sequence	Sect. 1.1	TDUP	Third Dredge-UP	Sect. 3.1
MS	Main Sequence	Sect. 1.1	(i)DUP	(i-th) Dredge-UP	Sect. 1.1
TAMS	Terminal-Age Main Sequence	Sect. 1.1	HBB	Hot Bottom Burning	Sect. 1.2
RGB	Red Giant Branch	Sect. 1.1	HBS	Hydrogen-Burning Shell	Sect. 1.1
RGBtip	Tip of the Red Giant Branch	Sect. 1.1	HeBS	Helium-Burning Shell	Chap. 4
ZACHeB	Zero-Age Core He-Burning	Sect. 1.1	HR	Hertzsprung-Russell (diagram)	Sect. 1.1
TACHeB	Terminal-Age Core He-Burning	Sect. 1.1	PDCZ	Pulse Driven Convective Zone	Sect. 1.2
AGB	Asymptotic Giant Branch	Sect. 1.1	TP	Thermal Pulse	Sect. 1.2
E-AGB	Early AGB	Sect. 1.2	EOS	Equation of State	Sect. 2.2
TP-AGB	Thermally Pulsing AGB	Chap. 1	MLT	Mixing-Length Theory	Sect. 2.2
WD	White Dwarf	Chap. 1	CMLR	Core Mass- Luminosity Relation	Sect. 4.1

Tab. 1: List of abbreviations used in the following, also with first appearance in the text.

Tab. 2: List of symbols used in the following, also with first appearance in the text. If not specified, the quantities are meant in CGS units.

Name	Description	First Appearance
α	mixing length parameter	Sect. 1.1
C	timestep and meshing parameter	Sect. 2.1
$\varepsilon_{\rm nuc}$	nuclear power produced per unit mass	Sect. 1.2
$f_{\rm ov}$	overshooting parameter	Sect. 2.2.3
F	local energy flux	Sect. 2.2.3

Tab. 1: (Continued)

Name	Description	First Appearance
[Fe/H]	metallicity	Sect. 2.3
∇	temperature gradient	Sect. 2.2.3
$\nabla_{\rm ad}$	adiabatic temperature gradient	Sect. 2.2.3
$\nabla_{\rm rad}$	radiative temperature gradient	Sect. 2.2.3
∇_{μ}	mean molecular weight gradient	Sect. 2.2.3
κ	Rosseland mean opacity	Sect. 1.3
H_P	pressure scale height	Sect. 2.2.3
M	star mass at the specified time	Sect. 1.1
M_i	initial star mass	Sect. 1.1
$M_{\rm bce}$	bottom mass coordinate of the convective envelope	Sect. 1.2
$M_{\rm He}$	mass coordinate of the H-free core (X-Y discontinuity)	Sect. 1.2
$M_{\rm CO}$	mass coordinate of the CO core	Sect. 1.2
m	mass coordinate of a spherical shell	Sect. 1.1
$\dot{M}$	absolute value of the mass loss per unit time	Sect. 1.3
$\eta_{\rm R}$	Reimers wind efficiency	Sect. 2.2.4
$\eta_{\rm B}$	Blöcker wind efficiency	Sect. 2.2.4
L	surface luminosity	Sect. 1.1
$L_{\rm H}$	luminosity produced by H-burning	Sect. 4.1
$L_{\rm He}$	luminosity produced by He-burning	Sect. 2.1
ℓ	local luminosity	Sect. 1.1
ρ	density	Sect. 2.2
P	pressure	Sect. 2.2
R	star radius	Sect. 1.2
$R_{\rm bce}$	bottom radial coordinate of the convective envelope	Sect. 1.2
$R_{\rm He}$	radial coordinate of the H-free core	Sect. 1.2
$R_{\rm C}$	radial coordinate of the CO core	Sect. 1.2
T	temperature	Sect. 2.2
$T_{\rm eff}$	effective temperature	Sect. 1.1
Y_i	number density of element i	Sect. 4.2
$X(i)$	mass fraction of element i	Sect. 2.2
X	hydrogen mass fraction	Sect. 2.2
Y	helium mass fraction	Sect. 2.2
Z	metals mass fraction	Sect. 2.2
μ	mean molecular weight	Sect. 2.2.3
$M_{\rm min}(i)$	minimum mass of the XY discontinuity after i-th pulse	Sect. 1.2
$M_{\rm max}(i)$	maximum mass of the CO core just before i-th TP	Sect. 4.1
$M_{\rm top}(i)$	top mass of i-th PDCZ at maximum extension	Sect. 1.2
$M_{\rm bot}(i)$	bottom mass of PDCZ i-th at maximum extension	Sect. 1.2
$\Delta M_{\rm He}$	H-free core growth during interpulse	Sect. 1.2

Tab. 1: (Continued)

Name	Description	First Appearance
$\Delta M_{\rm dup}$	mass involved in DUP	Sect. 1.2
$\Delta M_{\rm pdcz}$	PDCZ maximum extension	Sect. 1.2
$\Delta M_{\rm overlap}$	overlap between consecutives PDCZ	Sect. 1.2
λ	$= \Delta M_{\rm dup}/\Delta M_{\rm He}$, DUP efficiency	Sect. 1.2
r	$= \Delta M_{\rm overlap}/\Delta M_{\rm pdcz}$, overlap degree	Sect. 1.2
C/O	carbon-oxygen number ratio at surface	Sect. 1.2
t_i	star age at the i-th thermal pulse	Sect. 4.1

Name	Description	Value	First Appearance	Source
a	radiation density constant	$7.56578 \cdot 10^{-15}$ erg cm^{-3} K^{-4}	Sect. 2.2.3	CODATA
c	speed of light	$2.99792458 \cdot 10^{10}$ cm s^{-1}	Sect. 2.2.3	definition
$M_\odot$	mass of the Sun	$1.9892 \cdot 10^{33}$ g	Sect. 1.1	`MESA`
$L_\odot$	total luminosity of the Sun	$3.828 \cdot 10^{33}$ erg s^{-1}	Sect. 1.1	XXIXth IAU resolution B3
$R_\odot$	radius of the Sun	$6.957 \cdot 10^{10}$ cm	Sect. 1.2	XXIXth IAU resolution B3
$T_\odot$	solar effective temperature	5772 K	Sect. 2.2	XXIXth IAU resolution B3
$X_\odot$	protosolar H mass fraction	0.7154	Sect. 2.2	Asplund et al. (2009)
$Y_\odot$	protosolar He mass fraction	0.2703	Sect. 2.2	Asplund et al. (2009)
$Z_\odot$	protosolar metals mass fraction	0.0142	Sect. 2.2	Asplund et al. (2009)
$X_{\odot,ph}$	photospheric H mass fraction	0.7381	Sect. 2.2	Asplund et al. (2009)
$Y_{\odot,ph}$	photospheric He mass fraction	0.2485	Sect. 2.2	Basu & Antia (2004)
$Z_{\odot,ph}$	photospheric metals mass fraction	0.0134	Sect. 2.2	Asplund et al. (2009)
$R_{\rm cz}$	bottom radius of convective envelope	0.7133 $R_\odot$	Sect. 2.2	Basu & Antia (2004)

Tab. 3: List of (astro)physical constants used in the following, also with first appearance in the text. The atomic weights has been provided by NIST.

CHAPTER 1

Evolution of low- and intermediate-mass stars

This first chapter is dedicated to describe the evolution of low- and intermediate-mass stars from the PMS phase until the star has become a WD. Particular relevance is given to TP-AGB phase, which is the main scope of this work. In the chapter we will report many plots, constructed directly from the results of `MESA`; however, the details of the models will be discussed in the next chapters. The main references for the qualitative description of the evolution are given by Maeder (2009); Kippenhahn & Weigert (1990); Hansen et al. (2004).

1.1 From pre-main sequence to end core helium burning

Stars are formed from the collapse of a molecular cloud, and after a period of accretion, they reach a state in hydrostatic equilibrium, namely the pre-main sequence phase. The precise definition and what we mean for PMS starting point is matter of discussion in Sect. 2.3. In Fig. 1.1 the evolutionary tracks are showed for a low- and intermediate-mass prototype until TACHeB, both starting from the PMS phase.

At this point there are no active nuclear burnings and the star contracts to sustain the luminosity. This takes place along the Hayashi line relative to the particular M_i, because the structure is fully convective. The slow contraction however increases the temperature, the opacity decreases and the convective envelope recedes. The ZAMS (point A in Fig.1.1) is reached when hydrogen is ignited in the core. The channel through which H is destroyed depends on the mass, and this affects strongly the internal structure: for $M_i \lesssim 1.2 M_\odot$ hydrogen is depleted via the pp-chains, for which the luminosity produced per unit mass ℓ/m is small and the core stays radiative. Differently, for masses $M_i \gtrsim 1.2 M_\odot$, the central temperature is high enough for the CNO cycles, and the large ℓ/m produced causes the core to be convective.

When hydrogen is depleted in the center, TAMS (point B) is reached. The burning naturally proceeds in a shell around the radiative cores, but it is not the case for convective ones; the star must contract to increase the temperature, and eventually the hydrogen is still ignited in a shell. This produces the difference between the $1 M_\odot$ and $3 M_\odot$ tracks at the end of main sequence,

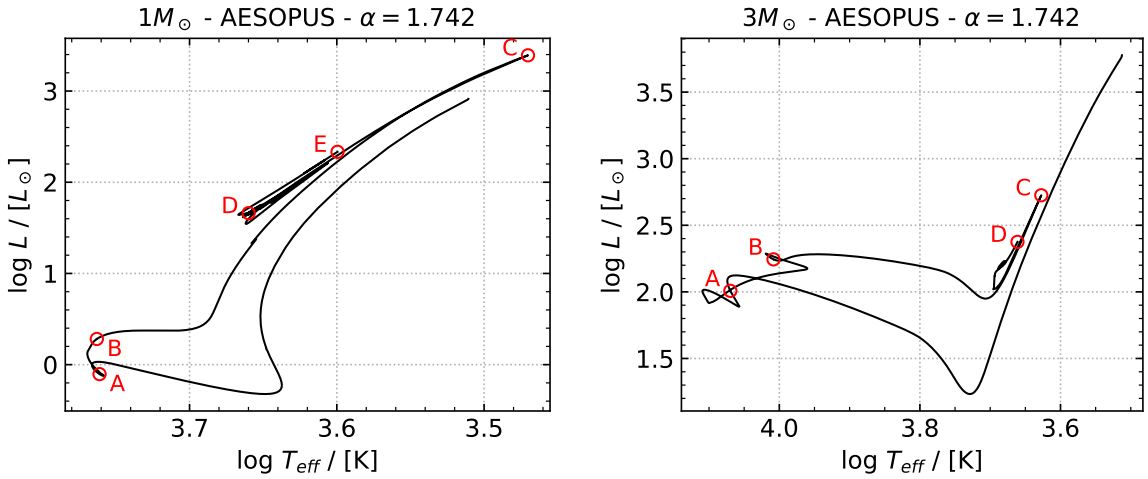

Fig. 1.1: Evolutionary track for $M_i = 1M_\odot$ and $M_i = 3M_\odot$, opacities from AESOPUS and $\alpha = 1.742$. The circles correspond, respectively, to ZAMS, TAMS, RGBtip, ZACHeB and TACHeB. For the $3M_\odot$ star, RGBtip and ZACHeB essentially coincide.

the latter has indeed a hook-like shape instead of a smooth transition. In any case, during the hydrogen shell burning, the star helium core is inert, it grows in mass and contracts; this is equivalent to say that the hydrogen burning shell moves towards higher mass coordinate and becomes thinner. The mirror principle dictates that the envelope must expand, decreasing the effective temperature. After point B this takes place at roughly constant luminosity; when the temperature is low enough and the structure is mostly convective, the expansion proceeds along the Hayashi line again, namely increasing the luminosity along the red giant branch.

While the star is in RGB phase the first episode of dredge-up takes place: the convective envelope extends deep in a region previously processed by core hydrogen burning, which has a different composition respect to the surface. The mixing event then changes the surface composition, which modifies the observed spectrum. The DUPs are also very important in the TP-AGB phase, and we will discuss some evolutionary details in Sect. 1.2 and more deeply in Chap. 4. Despite the evolution between B and C is qualitatively similar for low- and intermediate-mass stars, there is a relevant difference:

$M_i \lesssim 2M_\odot$: After MS, the electrons become degenerate in the core after it overcomes the Schömberg-Chandrasekhar limit (see Sect. 3.1). As the HBS gets thinner, the evolution speeds up and the core temperature increases, eventually up to $T \simeq 10^8$ K. At this point helium can be ignited, but in degeneracy conditions; this event starts a thermonuclear runaway, because the temperature can raise without expanding the core. In the HR diagram it coincides with the RGBtip (point C). The runaway causes a large production of energy, the He-flash; after the main flash, other smaller events can takes place and the degeneracy is completely lifted, reaching a quiescent core He-burning (ZACHeB, point D). The star runs again out of nuclear fuel, called TACHeB (point E).

$M_i \gtrsim 2M_\odot$: The core is not degenerate, and simply contracts to increase its temperature, until reaching the RGBtip. It roughly coincide with He-ignition, much in the same way hydrogen was ignited at ZAMS. During this phase of quiescent burning, intermediate-mass stars tracks

a loop in the HR diagram, essentially due to changing in the internal structure between mostly convective and radiative. The so-called blue loops are important because the stars evolve at nuclear timescale here, and thus this region is well populated. In the end the star goes again towards its Hayashi line, reaching its TACHeB.

1.2 The asymptotic giant branch phase

The evolution after the central He-burning for low- and intermediate-mass stars is qualitatively similar, so it is not worth anymore to consider $1M_\odot$ and $3M_\odot$ examples as completely separated. However, there are interesting events which seems to take place only above certain mass thresholds, despite being very model-dependent; these will be still highlighted in the following discussion.

The central He-burning proceeded through the 3α-reaction and $^{12}C(\alpha,\gamma)^{16}O$; when helium is exhausted, the core is composed mainly by carbon and oxygen. For $M_i \lesssim 8M_\odot$ the CO core is electron degenerate and further burning processes are avoided. Thus the core itself has ended its nuclear evolution, but the structure evolution of the star is very rich. Fig. 1.2 shows the internal structure of a star in this phase, precisely between E-AGB and TP-AGB. Going outwards from the center, we have the CO core surrounded by the He- and H-burning shell: between them there is an inert intershell mainly composed by helium. The star is then covered by a large convective envelope, due to large opacity and low temperature; since most of the structure is convective, the star climbs again the giant branch (the Hayashi line). A deeper look of Fig. 1.2 shows that the core of our prototype star (meaning everything but the envelope) is very compact, and it is indeed in a degenerate state: in mass coordinates the core mass amounts roughly to 20% of the total mass, while in radial coordinates it occupies only 0.4% of the total radius.

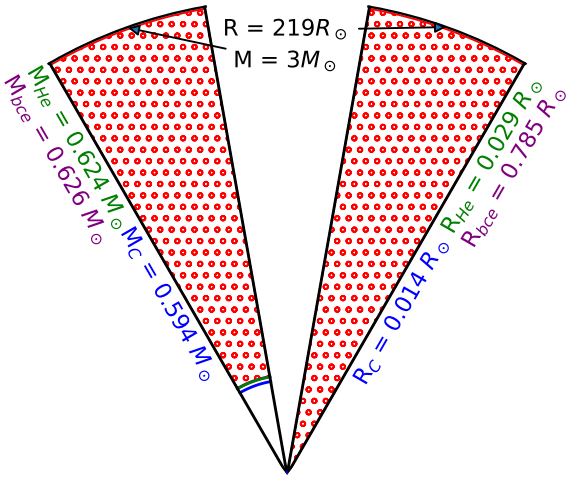

Fig. 1.2: Internal structure of a $M_i = 3M_\odot$ star in AGB phase, for mass (left) and radial (right) coordinates; proportions are preserved. Relevant values are also showed, and the circle hatching indicates convective region.

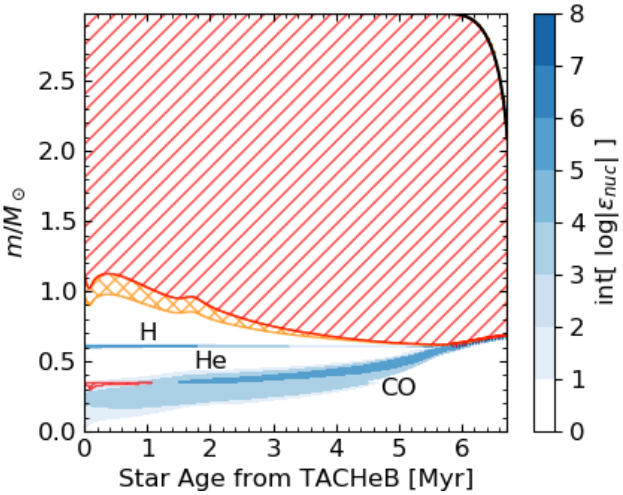

Fig. 1.3: Kippenhahn diagram for $M_i = 3M_\odot$ star in AGB. Red and orange hatch refer to convective and overshooting regions. The `int` in the colorbar means to take the integer part of the square brackets.

The E-AGB phase

The phase immediately after He-burning is called early AGB. Initially the star has the two burning shells and the mirror principle is valid on both of them. The CO core tends to contract, the He-rich intershell expands and the envelope contracts. The main effect is that the hydrogen shell is moved towards outer and cooler shells, and eventually shuts down. At this point the star has only the He-shell sustaining the luminosity, making $M_{\rm CO}$ increase. The H-shell power off and the CO core growth are both visible in Fig. 1.3. This phase is relatively long lived and quiescent; however for stars with large enough initial mass $M_i \gtrsim 4M_\odot$ the second episode of dredge-up can take place, when the convective envelope penetrates in a region previously interested by hydrogen shell burning. This event enriches the surface with the products of CNO cycles ^{4}He and ^{14}N, and mixes new hydrogen in regions where it was depleted; the latter is equivalent to say that the H-free core mass is reduced, effectively increasing the initial mass limit for those stars which can produce white dwarfs. For example, the Fig. 1.3 shows indeed that for a $3M_\odot$ star the second dredge up does not take place: the convective envelope reaches the shells previously involved in hydrogen burning, but it does not go deeper than that.

The TP-AGB phase

While He-shell is quiescently burning, it becomes thinner and moves outwards; at some point,

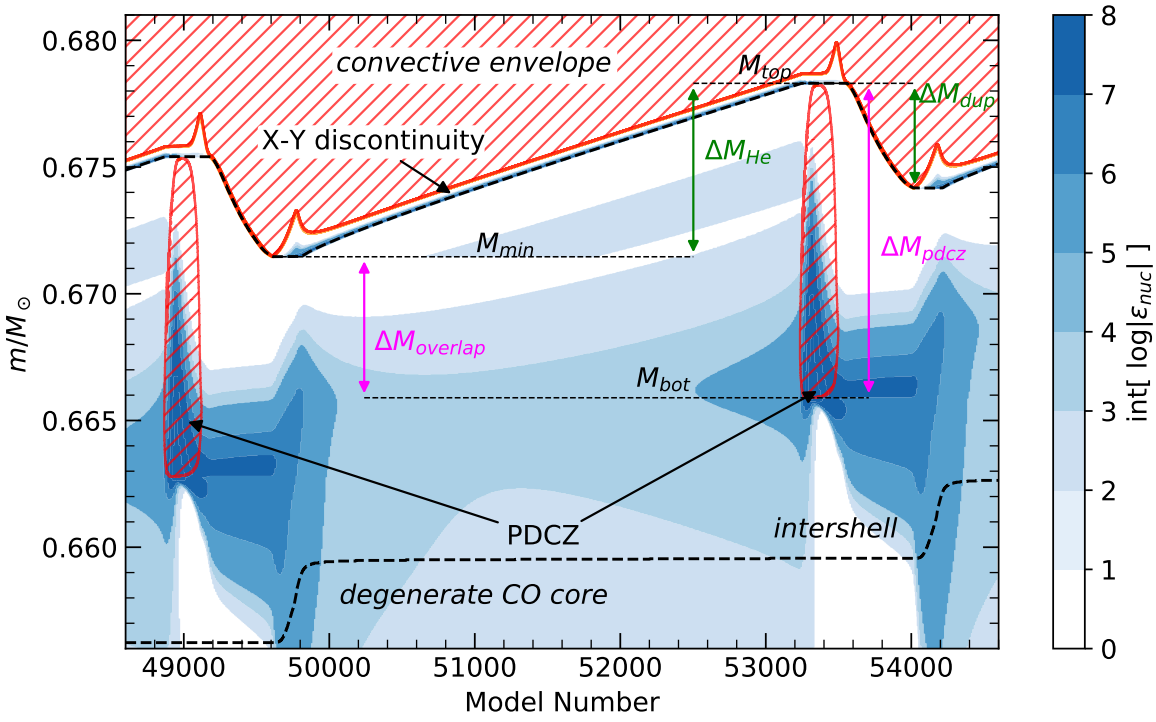

Fig. 1.4: Kippenhahn diagram zoomed around the intershell region, during the 14th and 15th thermal pulses of a $M_i = 3M_\odot$ star without overshooting in the PDCZ. The notation is explained in Tab. 2. Note that the region is extremely thin in mass coordinate, and even more in radial ones. We want to precise that during the interpulse the H-shell burns at a faster pace than the He-shell (and the latter is practically extinguished), but it cannot be appreciated in the figure due to the tiny scale. The x-axis reports the model number instead of the actual time for presentation purposes: the code naturally calculates shorter timesteps during the pulses, and the PDCZs in time coordinate would be extremely compressed.

the H-shell is ignited again but they never burn at the same pace. Note that both of these events are located near the end of the Kippenhahn diagram in Fig. 1.3. The helium shell soon suffer by the thin shell instability, which causes the thermal pulses: these are thermonuclear runaway in which, for a short amount of time, the He-shell produces a large amount of energy, much in the same way of the He-flash for helium ignition in degenerate condition, despite the different origin.

During the TP-AGB phase the star suffer many thermal pulses, and we can describe a cycle starting from a given TP:

TP: The thin shell instability triggers the thermonuclear runaway of He-burning when the intershell mass reaches a critical value; this event lasts for a short amount of time respect to stellar evolution timescales, in the range $10 - 100$ yr, as order of magnitude. The large production of energy per unit mass has two main consequences, visible in Fig. 1.4: (i) it forms a convective region called PDCZ; (ii) since it is mostly used for expanding the intershell region, the HBS is pushed towards outer and cooler regions, eventually shutting down. The "convective tongue" mixes the ^{12}C produced by the He-burning and the other elements in the intershell region.

3DUP: The expansion and the consequent cooling of the He-shell quickly quenches the pulse. The convective envelope can now move again inwards; eventually it penetrates even beyond the extinguished H-shell, entering in the intershell region and mixing the material present there. This mixing event is called third dredge-up; it is not expected to take place efficiently for every star under the mass range of consideration, nor from the very first thermal pulse. In particular, the occurrence depends strongly from the overshooting and convection parameters, but we can give $M_i \gtrsim 2M_\odot$ as a reference for now. The 3DUP efficiency is described by the parameter λ:

$$\lambda = \frac{\Delta M_{\rm dup}}{\Delta M_{\rm He}} \tag{1.1}$$

Differently from previous dredge-up episodes, which bring mainly ^{4}He and ^{14}N to the surface, the 3DUP mixes He-burning and s-process products. Note also that if $\lambda \simeq 1$ is equivalent to say that the H-free core (and then also the CO core) stops to grow in mass; this extreme case serves as example to observe that the 3DUP effectively limits the growth of $M_{\rm CO}$, allowing star of larger initial mass to become white dwarfs in the end. Taking the case reported in Fig. 1.4, the core still has a net growth even with DUPs; indeed $\lambda < 1$, but it is still able to limit the mass accretion, which would have been steeper without these events. The second relevant quantity to describe the evolution through the TP-AGB phase is the degree of overlap r:

$$r = \frac{\Delta M_{\rm overlap}}{\Delta M_{\rm pdcz}} \tag{1.2}$$

which is practically how much, in mass, two consecutive PDCZs overlap normalized to the size of the second. It turns out (Marigo et al., 2013) the intershell abundances are significantly dependent on r. In particular, when r smoothly declines the abundances are found to be stationary; instead if r varies more rapidly, the intershell composition changes.

interpulse: After the potential dredge-up phase, the H-shell is ignited again, while the He-shell becomes practically inactive. In the Fig. 1.4 we can see that the hydrogen re-ignition causes a temporary recession of the convective envelope and also that the intershell region grows in mass with the ashes of burning shell. The typical time duration of this phase depends on the core mass, varying from about $10^3 - 10^5$ yr for decreasing $M_{\rm CO}$.

The TP-AGB phase has a very rich chemical and abundances evolution: 3DUP events directly change the surface composition, which can be also seen by observations; in addition the AGB star environment is suitable for unique nucleosynthesis. We have already stressed that the third dredge-up brings He-products to the surface, in particular ^{12}C, changing the C/O ratio and the spectral type: M-type collects the stars with C/O < 1; C-type includes the carbon stars, namely those with C/O > 1; the intermediate case corresponds to the S-type. Besides the carbon-to-oxygen ratio, in TP-AGB stars the s-process is active, producing elements also beyond iron group. To do that, the star needs neutron: the source can be found in the ^{13}C$(\alpha,\mathrm{n})^{16}$O and ^{22}Ne$(\alpha,\mathrm{n})^{25}$Mg reactions. Last but not least, if the star initial mass is large enough, the H-burning can be ignited in the base of the convective envelope. This process is called hot bottom burning, and it should take place for $M_i \gtrsim 4-5M_\odot$. A comparison between two models is given in Fig. 1.5. The bottom line of this process, besides other spectral modifications, is to prevent stars becoming C-type.

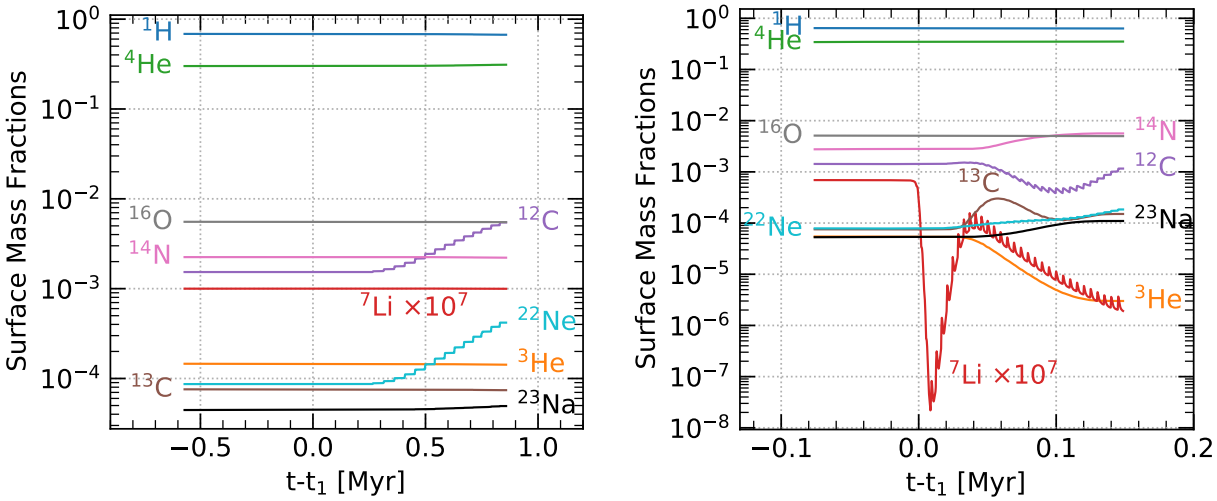

(a) Initial mass $M_i = 3M_\odot$

(b) Initial mass $M_i = 5M_\odot$

Fig. 1.5: Surface mass fractions of labeled elements for two models with different mass. They have a very different morphology, mainly because the HBB is active in the $5M_\odot$ star. We do see indeed that in (a) ^{12}C and ^{22}Ne are accumulated and the star is extremely poor in ^{7}Li; instead in (b) the HBB convert the carbon and neon into ^{14}N and ^{23}Na. In addition the ^{7}Li present in the pp-chains can be moved outwards by convection, preventing its destruction, but also it can be moved inwards. The result is a temporary super-rich phase of ^{7}Li. In conclusion, note that at some point in (b) ($t - t_1 \sim 0.1$ Myr) the HBB is practically shut down, accumulating again ^{12}C and ^{22}Ne.

1.3 Mass loss and post-AGB evolution

The dramatic changes suffered by the star during the TP-AGB phase are not only due to the recurrent thermal pulses. This stage of the evolution is also characterized by a strong stellar wind, which can erode the envelope at a fast pace from $\dot{M} \simeq 10^{-8}\ M_\odot\ \mathrm{yr}^{-1}$ to $\dot{M} \simeq 10^{-4}\ M_\odot\ \mathrm{yr}^{-1}$. The stellar wind is mainly driven by radiation pressure on dust grains, assisted by dynamical pulsations of the stellar surface. Indeed AGB stars have cool atmospheres, in which the gas particles can condense into dust grains, which are very opaque to radiation; however the sole radiation momentum transfer to the grains is not enough to explain the large mass losses expected for AGB stars, and pulsations are thought to play a key role. The TP-AGB phase duration for low- and intermediate- mass is indeed determined by the mass loss; when the hydrogenic envelope is left with a mass $\simeq 10^{-2} - 10^{-3} M_\odot$, or equivalently when the H-burning shell is pushed to a mass coordinate of $10^{-2} - 10^{-3} M_\odot$ from the surface, the star leaves the AGB.

In the post-AGB phase the star shrinks its radius and increases temperature at almost constant luminosity, which is still powered by the leftover H-burning shell. The star reaches very high $T_{\rm eff}$, radiating in UV band and ionizing the circumstellar envelope (namely all the mass previously ejected), appearing as a planetary nebula. Since the stellar wind is still active, at some point the hydrogen burning shuts down and the star slowly cools down as a white dwarf, towards fainter luminosity. Interestingly, in the post-AGB phase or even in the initial phase of the WD cooling, the star can experience a final thermal pulse, temporarily bringing back the star in the AGB part of HR diagram. Two examples are reported in Fig. 1.6, showing the evolution from the E-AGB phase to WD, stopping at $\log L/L_\odot = -2$.

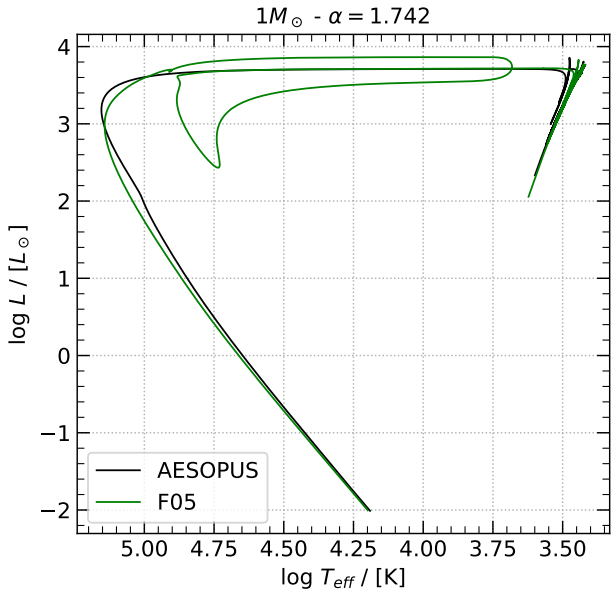

Fig. 1.6: Two evolutionary tracks for a $M_i = 1 M_\odot$ star from AGB to WD phase, with different opacity. The one with $\kappa_{\texttt{F05}}$ experience the "born-again" scenario cited in the text, temporarily going back near the AGB region of the diagram. The opacity `F05` are taken from Ferguson et al. (2005).

CHAPTER 2

The MESA stellar evolution code

The second chapter is devoted to everything concerning the stellar evolution code. First of all, we give a brief description of MESA and its advantages. Then we explore the adopted physics for the models calculated of the thesis and in conclusion we discuss the solar calibration of the parameters. For this work we use MESA version 12778, compiled with GNU Fortran (GCC) 9.2.0 installed as a part of the MESA SDK version 20.3.1.

2.1 Introduction to MESA

MESA[1] is a open-source stellar evolution code, widely used for research and educational activities. It is undergoing active development and we refer to Paxton et al. (2011, 2013, 2015, 2018, 2019) for further and more detailed information about the code and its capabilities. The package is organized in modules, each one focused to different aspect of the stellar evolution, for example the 1D solver for the structure and evolution equations, the opacity, nuclear network calculations and so on. The modularity is a clear advantage for many reasons: (i) it makes the code very flexible and suitable for many purposes, from stellar evolution to accretion onto compact objects or giant gas planet evolution; (ii) the runs usually utilize only a part of the modules, which makes it faster to execute; (iii) planned modifications can be performed on the single modules, which makes them simpler and safer from corruption risks.

The core module for our models is the 1D stellar evolution module, called MESA star. It is designed to solve the structure and evolution equations via a Netwon-Raphson method; the system of equations is non linear and involves a large number of variables. The focus of this work is not about the numerical details inside MESA; however in order to develop meaningful and detailed models one has to know qualitatively how the code works. The algorithm tries to solve the equations within a selected timestep and mesh adjustment, which is chosen at the beginning. If the system converges within the user-selected precision, related to the difference between the actual model and the previous one, the solution is accepted and the calculation proceeds further;

[1] It is available to download from http://mesa.sourceforge.net/.

on the opposite case, MESA tries again with a reduced timestep, calling a "retry". Subsequent retries cause the algorithm to return on the previous model with a smaller timestep, calling a "backup"; this sequence continues until convergence or a pre-defined timestep minimum, at which point the evolution is stopped without finding a successful model.

Clearly the user can manipulate the timestep and meshing parameters, besides the input physics which is discussed in Section 2.2. In this respect, the most important parameters are varcontrol_target and mesh_delta_coeff: the first measures the target residual for the variables within two models; the second allows to control the mesh points in the structure. We use the notation introduced in Paxton et al. (2011): the two parameters are modified by multiplying them with the same coefficient C. Default values are selected $C = 1$, while $C < 1$ means to seek for smaller residuals (usually requiring smaller timesteps) and more mesh points. Setting a small C increases the model accuracy but the computation time is considerably longer; for this reason we try to choose the largest C without compromising the quality of the models. In Choi et al. (2016) it is reported that for low- and intermediate-mass stars the relative differences between models with $C = 2$ and $C = 1/8$ is within few percent. The user can also add more refined timestep and mesh adjustment, for example limiting the variation of a quantity within two models or adjacent mass shells. This is extremely useful in some moments of the evolution or in particular regions in the star's interior.

Parameter modification and choice are collected in the inlist files, which are read at the start of the evolution. New or modification to the code routines are instead written in a FORTRAN module called run_star_extras.f, without modifying the original MESA files. In this work we divided the star evolution into four inlist files, to better adjust the timestep and meshing points for the different phases:

(P1) The first phase is considered from PMS to TAMS. Here we just choose $C = 1/2$, which is a good compromise between model quality and execution time.

(P2) The second phase goes from TAMS to TACHeB. For low-mass stars, which suffer from He-flash, we take $C = 1$ but limiting the variation of $L_{\rm He}$ in order to have a good accuracy near the flashes. For the intermediate-mass case instead we leave $C = 1/2$.

(P3) The third phase corresponds to the AGB. Here we tried both $C = 1$ and $C = 1/2$ for the majority of models. However we are interested in have a good resolution in the intershell region, so we add more mass shells in the burning regions and around the overshooting ones[2]. In addition we inserted mass shells in regions with gradients in H, ^{4}He, ^{13}C and ^{14}N in order to have an higher resolution near the X-Y discontinuity, which is relevant for the third dredge-up. For timestep, we limit the variation to $L_{\rm He}$ and to absolute and relative variation of hydrogen abundance: the first constraint allows to have a good temporal resolution during pulses, the second instead tends to calculate smaller timesteps during the interpulse phase where the hydrogen burning dominates.

(P4) The last phase collects the post-AGB and WD cooling evolution. Here we set $C = 1$.

[2]This feature is added into run_star_extras.f, since it is not present in the main routines. It can be found in one of the test cases, called agb, present in the code installation.

We have presented our general approach to reproduce our models. There could be minor tweaks which are not listed here, but they should not compromise the reproducibility of our results, since they are aimed only to reduce the number of retries and speed up the calculations for particular cases.

2.2 Models input physics

2.2.1 Chemical composition, opacity and equation of state

Composition. First of all we need to specify the chemical mixture. Our reference scale is of course given by the element distribution of the Sun; in this respect, we choose the abundances given in Asplund et al. (2009). As it is recommended in that work, we discriminate between the photospheric and protosolar abundances (see Tab. 3); that is because of diffusion, which causes the heavy elements to stream down from the photosphere. In Asplund et al. (2009, Tab. 1) the fractional abundances $X_\odot(i)/Z_\odot$ of the 90 metals from Li to U in the present-day photosphere are collected; as already pointed out, $X_{\odot,ph}$, $Y_{\odot,ph}$ and $Z_{\odot,ph}$ are sensibly different due to diffusion. However the element-to-element diffusion is estimated to be much less pronounced and even not currently testable; indeed the metals distribution inside $Z_\odot$ is retrieved directly from the photospheric fractions. Every model computed for this work is solar-scaled, meaning that the input X, Y, Z and the metal distribution are equal to the protosolar abundances. The only exception is present in Section 2.3, where I refer for a detailed discussion.

EOS. In `MESA` the equation of state is characterized by a set of density-temperature tables, which essentially give all the thermodynamic quantities (such as pressure, internal energy, entropy etc.) as a function of (ρ, T) couples. The `MESA` tables are based on the 2005 update of OPAL tables (Rogers & Nayfonov, 2002) gradually switching to SVCH tables (Saumon et al., 1995) at lower temperature and density. They cover the cases $X = (0.0, 0.2, 0.4, 0.6, 0.8, 1.0)$ and $Z = (0.0, 0.02, 0.04)$, while for $Z > 0.04$ and low densities the PTEH tables are used (Pols et al., 1995). Outside that spanned region (high density and high temperature) HELM (Timmes & Swesty, 2000) and PC (Potekhin & Chabrier, 2010) are employed, which assumes complete ionization and, respectively, take into account effects as electron-positron pair creation or crystallization. More details are given specifically for the EOS are given in Paxton et al. (2011, 2019), in particular see Paxton et al. (2019, Fig. 1) for a visual summary.

Opacity. The interaction properties of matter with radiation are described by the opacity κ, frequency averaged as in the Rosseland approximation in the radiative transport equation. The opacity is a function of ρ, T and chemical composition; it is pre-computed and stored in tables, as the EOS, then the choice has to be coherent with the selected chemical composition. `MESA` divides the opacity tables in two regimes, for low and high temperature. The default transition region is set at $3.80 \leq \log T \leq 3.88$. We use OPAL opacity tables (Iglesias & Rogers, 1993, 1996) for the high T regime and ÆSOPUS tables (Marigo & Aringer, 2009) for the lower temperatures, both of which are already available in `MESA` for the chosen chemical composition. A further distinction is made for the high temperature tables; the user can select between Type I and II opacities, the first being for a fixed metal distribution and the latter accounts for the variation of carbon and oxygen abundances. For simplicity we set the Type II tables for the whole

evolution, even if they have a lower resolution in X and Z. That is because we are interested mainly in the AGB phase, in which the mixing events continuously change the abundance of C and O throughout the structure.

2.2.2 Nuclear reactions

`MESA` collects thermonuclear reaction rates from Caughlan & Fowler (1988, CF88), Angulo et al. (1999, NACRE) and JINA REACLIB database (Cyburt et al., 2010). By default the preference is set for NACRE rates, with significant updates listed in Paxton et al. (2011); if a reaction rate is not present there then CF88 or JINA REACLIB is used. We chose to leave the default settings, because the work is focused to explore different overshooting schemes and mass loss; the comparison between the different presented cases are valid for any set of reaction rates, being recent or outdated. The thermonuclear network traces the abundance evolution N = 29 species: n, ^{1}H, ^{2}H, ^{3}He, ^{4}He, ^{7}Li, ^{7}Be, ^{8}B, ^{12}C, ^{13}C, ^{13}N, ^{14}N, ^{15}N, ^{16}O, ^{17}O, ^{18}O, ^{19}F, ^{20}Ne, ^{21}Ne, ^{22}Ne, ^{21}Na, ^{22}Na, ^{23}Na, ^{24}Mg, ^{25}Mg, ^{26}Mg, ^{25}Al, ^{26}Al, ^{27}Al. All the reactions are listed in the default file `sagb_NeNa_MgAl.net`, which essentially includes pp chains, CNO cycles (hot and cold), triple-α reaction and α captures up to ^{24}Mg, Ne-Na cycle and Mg-Al cycle. The code also calculates the electron screening both in weak and strong regimes; the default `MESA` option calculates the screening factors as described in Chugunov et al. (2007).

2.2.3 Mixing processes

Convection. In stellar interiors convection is based on the mixing-length theory, which parameterize the distance traveled by a convective bubble via the pressure scale height H_P:

$$d = \alpha H_P \qquad\qquad H_P = \left| \frac{\mathrm{d} \ln P}{\mathrm{d}r} \right|^{-1} \tag{2.1}$$

α is the mixing-length parameter, and it measures the efficiency of convection. Being a parameter, it needs to be calibrated or assigned to a value a priori; that is because we have no way to express it as a function of stellar observable properties. The recipes given by MLT clearly oversimplify the problem, which is naturally related to a fluid in turbulent regime, and it has its own pros and cons. The results of mixing-length theory are relatively easy to implement in a code compared to hydrodynamic simulations, but the resulting models strongly depend by the various user-provided parameters. Nevertheless it is an essential tool to achieve a proper description of the stellar structure and evolution. The convective processes induce a mixing of material and a different way to transport energy that is not radiation. The mixing events are described as a diffusion processes, while the energy transport is calculated via a convective flux F_{conv} which depends on α. In `MESA` the MLT is implemented with different prescriptions; we selected the MLT version of Henyey et al. (1965), which does not assume large optical depths and it accounts for radiative losses from the convective bubbles, important for regions near the surface. This adds two free parameters, which are left to their default and recommended values $\nu = 8$ and $y = 1/3$; respectively, they multiply the convective velocity and temperature gradient of the eddies. Instead α has been calibrated to reproduce the observable solar properties, for which I refer to Section 2.3.

The stability against convection is usually investigated using the Schwarzschild criterion:

$$\nabla_{\rm rad} < \nabla_{\rm ad} \tag{2.2}$$

where the radiative temperature gradient is defined as the (fictitious) temperature gradient needed to carry the whole energy flux:

$$F = F_{\rm conv} + F_{\rm rad} = \frac{4acT^4}{3\kappa\rho}\frac{\nabla_{\rm rad}}{H_P} \tag{2.3}$$

The radiative flux has an equivalent definition, substituting the actual temperature gradient $\nabla = \mathrm{d}\log T/\mathrm{d}\log P$ to the radiative one. $\nabla_{\rm ad}$ is again the temperature gradient but calculated assuming adiabatic conditions. If the inequality (2.2) is satisfied then the medium is convectively stable. However, the Schwarzschild criterion has to be modified to account for a chemical composition gradient:

$$\nabla_{\rm rad} < \nabla_{\rm ad} - \frac{\chi_\mu}{\chi_T}\nabla_\mu \tag{2.4}$$

where we used the definitions:

$$\chi_\mu = \left(\frac{\partial \log P}{\partial \log \mu}\right)_{\rho,T} \quad \chi_T = \left(\frac{\partial \log P}{\partial \log T}\right)_{\rho,\mu} \quad \nabla_\mu = \frac{\mathrm{d}\log\mu}{\mathrm{d}\log P} \tag{2.5}$$

The inequality (2.4) is called Ledoux criterion, which reduces to the Schwarzshild one in case of homogeneous medium. Should one use (2.2) or (2.4)? The question naturally arises because in the literature the choice seems arbitrary, but clearly it is not. Convective regions have homogeneous composition due to mixing, then inside these shells Ledoux and Scwharzschild criteria are the same. Problems arise in the boundaries between radiative and convective regions, and their implementation in numerical codes. A detailed discussion is given by Gabriel et al. (2014), but since the two criteria coincide in the convective side of the boundary the question is physically meaningless and concerns only numerical techniques. As a matter of fact, the Ledoux criterion more often leads to problems, and we will briefly discuss one of the effects of using it in the AGB phase.

Finally, we use the Ledoux criterion for the whole evolution up to AGB, where we switch to Schwarzschild crterion. The reasoning behind this particular choice is hinted just above, but it will be clear in the following.

Overshoot. As it is so far, convection seems quite unnatural; Ledoux or Schwarzshild criteria would imply that a convective blob has to instantaneously stop its motion at the convective boundary. The element has to overshoot in a, theoretically, non-convective region just by inertia. It turns out that the convective overshoot is extremely important for the stellar structure and evolution, for example during the TP-AGB (Herwig, 2000). We will also see in this thesis the effect of different overshoot schemes.

However only the MLT does not predict such behavior; a new set of free parameters are required, which have to be guessed or calibrated, and they depend on the overshoot prescription; in `MESA` there are two available. The first method is called step overshoot and it simply extends the mixing region by a given fraction of H_P; the physical idea is clear (Bressan et al., 1981): $\nabla_{\rm rad} = \nabla_{\rm ad}$ corresponds to the point where the convective element acceleration is zero, however

the mixed region extends up to where the velocity vanishes. An example of application of this formalism is found in the PARSEC stellar evolution code (Bressan et al., 2012). The second scheme, which is used in the models for this thesis, is called exponential overshoot. This prescription is motivated by the behavior of convective elements seen in radiation hydrodynamic simulations of Freytag et al. (1996), and the parameters involved are described by Herwig (2000) and Choi et al. (2016). The main ingredient is the diffusion coefficient in the overshooting region:

$$D_{\rm ov}(r) = D(0)\exp\left(-\frac{2r}{H_v}\right) \qquad \text{for} \qquad H_v = f_{\rm ov}H_P \tag{2.6}$$

where H_v is the velocity scale height, parametrized as a fraction of the pressure scale height. The distance r is calculated from a depth $f_{0,\rm ov}H_P$ from the convective border, which corresponds to the point where the diffusion parameter is equal to $D(0)$. The exponential overshoot then adds two free parameters $(f_{\rm ov}, f_{0,\rm ov})$. I follow the same assumption of Choi et al. (2016), taking $f_{0,\rm ov} = 0.5 f_{\rm ov}$, effectively reducing the number of free parameters by one. I divide the overshooting into three sets of $(f_{\rm ov}, f_{0,\rm ov})$:

- *Core overshooting*: applied on the outer boundary of convective cores. We fix this couple to $(0.016, 0.008)$ as done by Choi et al. (2016).
- *Envelope overshooting*: applied on both boundaries of the convective envelope. We calibrate the associated $f_{\rm ov}$ in Sect. 2.3.
- *PDCZ overshooting*: applied on both boundaries of the PDCZ. A more extensive discussion and different couples of parameters are explored in Sect. 4.2.

Semiconvection. Analyzing the Ledoux criterion clearly shows that the composition gradient ∇_μ (typically positive, and $\chi_\mu = -1$ for an ideal gas) has a stabilizing effect and prevent some layers to be formally convective, which they would be unstable for the Schwarzschild criterion. In formulas:

$$\nabla_{\rm ad} < \nabla_{\rm rad} < \nabla_{\rm ad} - \frac{\chi_\mu}{\chi_T}\nabla_\mu \tag{2.7}$$

These layers are said to be semiconvective and they are interested by mixing, even if weaker than the purely convective regions where the composition is homogeneous. Indeed this process is treated in a diffusion approximation, introducing a new free parameter $\alpha_{\rm sc}$ to parametrize the efficiency of this effect. MESA uses the treatment of semiconvection described by Langer et al. (1985). In the same work they show that semiconvection can modify the duration of the red supergiant phase of massive star, or even changing the ratio between red and blue supergiant stars. For low- and intermediate-mass stars the main effect is to change the size of convective cores during the main sequence, as discussed by Paxton et al. (2013). The models for this work include semiconvection with $\alpha_{\rm sc} = 0.1$ (Choi et al., 2016) in all evolutionary stages where the Ledoux criterion is used.

Thermohaline mixing. Semiconvective mixing refer to $\nabla_\mu > 0$, which is also the usual condition since nuclear reactions tend to create particles with larger mass in the center. However in stellar interior a negative mean molecular weight gradient can build up. If that is the case, also supposing that the layer is stable (otherwise it is convective), we have a double diffusive

mechanism: heat tends to diffuse to outer layers, while the heavier particles ("salt") tends to diffuse to the interiors. This is called thermohaline mixing; this process turns out to be very important to explain variation of surface abundances after the first dredge-up, which cannot account for the whole changes. More details about thermohaline mixing are given by Charbonnel & Zahn (2007) and later in this work. In `MESA` there are three available prescription for this process, but we set the one from Kippenhahn et al. (1980); similarly to semiconvection, another free parameter needs to be introduced to describe the efficiency. We take it $\alpha_{\rm th} = 666$, as suggested by Choi et al. (2016, and references therein), which seems to be the appropriate value to reproduce the non-canonical mixing found in observations of low-mass RGB stars.

Diffusion. With the `diffusion` module, `MESA` accounts for microscopic diffusion, gravitational settling and radiative levitation. The code solves the Burgers' equations (Burgers, 1969) with the modifications introduced by Hu et al. (2011) to account for an extra force from the radiation pressure. However we do not account for radiative levitation in the models; that is because the calculation is very costly and the effect on low- and intermediate-mass stars should be limited (Turcotte et al., 1998), since radiation pressure is not dominant. I already cited the importance of including chemical diffusion in stellar models in Subsect. 2.2.1, for which I select the default `MESA` options: the diffusion coefficients are taken from Stanton & Murillo (2016) and to speed up the calculation keeping a good accuracy, the elements are grouped into 5 classes. These groups are represented by ^{1}H, ^{3}He, ^{4}He, ^{16}O, ^{56}Fe and each of them collects the element with atomic number up to the class representative. At each class is then assigned a typical charge, as described by Thoul et al. (1994). Finally, diffusion is expected to have no or little effect when more efficient mixing processes, such as convection, are present and when the evolutionary timescale is shorter than the typical diffusion time. For this reason, diffusion is included only during the main sequence of our models, because in post-MS phases the convective envelope accounts for most of the star extension.

2.2.4 Mass loss

Mass loss due to stellar winds is a fundamental part of the star evolution of all masses. For low and intermediate-mass stars is mostly relevant in the post-MS phases, while during the main sequence the star is expected to have almost no variation in mass. At the present day, the mechanism driving winds in AGB phase is reasonably known: these stars have cool atmospheres where the gas, moved upward by pulsations, can condense into dust grains and eventually it is pushed away by radiation pressure. Instead, the wind mechanism for RGB stars is still a matter of debate (Harper, 1996; Willson, 2000; Miglio et al., 2012).

In stellar evolution codes it is customary to implement the mass loss via empiric formulas, which depends on global stellar properties. For RGB phase we use the Reimers prescription (Reimers, 1975):

$$\dot{M}_{\rm R} = 4 \times 10^{-13} \eta_{\rm R} \frac{(L/L_\odot)\,(R/R_\odot)}{(M/M_\odot)} \quad {\rm M_\odot\ yr^{-1}} \tag{2.8}$$

Instead for AGB we employ the Blöcker formula (Blöcker, 1995):

$$\dot{M}_{\rm B} = 4.83 \times 10^{-9} \eta_{\rm B} \frac{(L/L_\odot)^{2.7}}{(M/M_\odot)^{2.1}} \frac{\dot{M}_{\rm R}}{\eta_{\rm R}} \quad {\rm M_\odot\ yr^{-1}} \tag{2.9}$$

Equations (2.8) and (2.9) contain two free parameters, $\eta_{\rm R}$ and $\eta_{\rm B}$; they quantify the efficiency of the Reimers and Blöcker wind, respectively. Typical values for the Reimers efficiency span the interval 0.1-0.5 and η_B is commonly one order of magnitude less (Choi et al., 2016; Miglio et al., 2012; Pignatari et al., 2016). We assume $\eta_R = 0.35$ and the following for Blöcker wind: (i) solar-mass models use $\eta_B = 0.01$; (ii) $M_{\rm i} < 3M_{\odot}$ models are computed with $\eta_B = 0.02$; (iii) $M_{\rm i} \geq 3M_{\odot}$ have $\eta_B = 0.03$. This particular choice is motivated by a compromise between a reasonable computational time and avoiding a too fast envelope dispersion. Note also that these empirical recipes are insensible to the actual wind mechanism and surface composition. Especially the carbon-to-oxygen ratio C/O alters completely the opacity and the dust composition in the atmosphere, affecting the wind magnitude. Recent works are adopting different prescriptions (Marigo et al., 2013, references therein), regulating $\eta_{R,B}$ values during the evolution to the present C/O ratio (Pignatari et al., 2016) or extracting new prescription from radiation hydrodynamic simulations, showing a composition dependence (Mattsson et al., 2010; Eriksson et al., 2014; Bladh et al., 2019). Mass loss is one of the most important aspect for the AGB phase, since it can dramatically affect the duration and the mass of the final remnant.

2.2.5 Boundary conditions and what is missing

In order to solve the stellar structure and evolution equations boundary conditions has to be provided for temperature and pressure for the outermost shell of the model. A plane-parallel atmosphere in the Eddington approximation is commonly used, but in this work we follow the same choice made by Choi et al. (2016, discussion therein); since we deal with low- and intermediate-mass stars `photosphere_tables` are used.

Finally I want to give a brief description of the missing physics in our models. For simplicity we decided not to include rotation for two reasons:

- Rotation is another challenging problem to deal with, which details are still not well understood. We do know that the effect is very important for massive stars, while it is limited for low- and intermediate-mass stars. I also point that during AGB phase rotation is even less important, just for angular momentum conservation; to see that, one can fix the rotational velocity during the main sequence, where the radius is relatively small. When the star is then placed in the RGB or AGB phases, the radius is much larger thus the rotation velocity is way smaller.

- Rotational effects include further mixing and wind enhancement, both of which add a bunch of new free parameters. These should be carefully set, in order to produce physically-sound stellar models. In this work, we prefer to limit the parameter space for simplicity, being aware of the first reasoning.

Lastly, `MESA` currently does not implement magnetic field effects. They are observed near the stellar surface, then they should have some impact on the structure and evolution. Magnetic fields can couple to rotation and produce stellar winds, and there is a lot of effort going on to study the effects and implement them, as for rotation. A more extensive discussion about rotation and magnetic fields is given by (Choi et al., 2016, and references therein).

2.3 Solar calibration

In the previous discussion I mentioned the calibration of α and $f_{\rm ov}$ on the solar current surface and helioseismic properties; these are summarized in Tab. 2.1. For this purpose I employ the `MESA` routine `simplex_calibration`, which counts up to five free parameters: initial metallicity $[\mathrm{Fe/H}]_i$, intial helium surface abundance Y_i, mixing-length parameter α, envelope overshooting efficency $f_{\rm ov}$ and initial mass M_i. The metallicity at any time is defined as:

$$[\mathrm{Fe/H}] = \log\left(\frac{Z}{X}\right) - \log\left(\frac{Z_{\odot,ph}}{X_{\odot,ph}}\right) \tag{2.10}$$

Once Y_i and $[\mathrm{Fe/H}]_i$ are known, the hydrogen initial abundance is known from the normalization $X_i + Y_i + Z_i = 1$. Since the calibration is based on the current solar properties, the mass is fixed to $1M_\odot$. However for this purpose we have to define what we mean as current properties, namely we need to know the age of the Sun $t_\odot$. From a theoretical point of view the age is counted from the start of PMS, which is defined as when the central temperature is $T_c = 3 \cdot 10^5$ K in the `MESA` default settings. Nevertheless we do need the observational counterpart, which measurement is possible studying number ratios of radioactive elements and meteorites (Bahcall et al., 1995); they also give $t_\odot \simeq 4.57$ Gyr as result. However it is not clear to what stage of pre-main sequence solar evolution this age represents, being near the end when the Sun is approaching ZAMS, or the very start. The time spent in PMS phase by a solar-like star is $(3-4) \cdot 10^7$ yr (Bahcall et al., 2006), quantifying the systematic uncertainty of the age reference. In this work I adopt the same choice given in the `MESA` calibration routine, namely considering the age of the Sun equal to $t'_\odot = 4.57 + 0.04$ Gyr. In any case, the difference between the quantities at $t'_\odot$ and $t_\odot$ is reasonably small, as confirmed by Bressan et al. (2012). Having addressed this issue, the routine works as follows: (i) values for the four free parameters are drawn from a given interval; (ii) a solar mass star is evolved up to $t'_\odot$; (iii) the model is rated with a χ^2 method, involving surface and helioseismic quantities (see Tab 2.1), with user defined tolerances; (iv) the procedure is repeated until the χ^2 reaches a stable minimum, ideally equal to the number of target parameters. The results of the best-fit model are collected in Tab. 2.1; surface properties are accurately reproduce however the helioseismic inferred ones, surface helium abundance and bottom radius of the convective envelope, are not. This is a known tension in solar-scaled models when using the Asplund et al. (2009) chemical

Parameter	Target	Value	Relative error (%)
$L_\odot$ (10^{33} erg)	3.828	3.8262	$4.6 \cdot 10^{-2}$
$T_\odot$ (K)	5772	5774.1	$3.6 \cdot 10^{-2}$
$R_\odot$ (10^{10} cm)	6.957	6.9601	$4.5 \cdot 10^{-2}$
$[\mathrm{Fe/H}]_{ph}$	0.0000	-0.0005	$5.7 \cdot 10^{-2}$
Y_{ph}	0.2485	0.2259	9.1
$R_{\rm bce}$ ($R_\odot$)	0.7133	0.7333	2.8
X_{ph}	0.7381	0.7603	3.0
Z_{ph}	0.0134	0.0138	2.8
X_i	0.7154	0.7353	2.8
Z_i	0.0143	0.0149	4.6
Y_i	0.2703	0.2498	7.5
$[\mathrm{Fe/H}]_i$	0.0418	0.0496	18
α	...	1.7427	...
$f_{\rm ov}$	...	0.0320	...

Tab. 2.1: The table is divided in three sectors. From above, the first sector shows the quantities entering the χ^2 method; the second shows other calibration-derived properties not involved in the χ^2 calculation; the third collects the free parameters values at the end of calibration, with their solar observed values if present.

composition. In particular Choi et al. (2016) also finds a very small amount of initial helium, which is comparable to the Big Bang primordial abundance $Y_p = 0.247$ (Planck Collaboration, 2018); this is clearly non-physical, since the Sun is a population I star. The discrepancy propagates on the surface helium abundance calculated at $t'_{\odot}$, which is much lower than the helioseismologically value measured by Basu & Antia (2004). Interestingly we found present helium abundance similar to Bahcall et al. (2006) for their solar model with Asplund et al. (2005) chemical abundances; this can be reasonable, since we did not include sound speed profile in the χ^2 calculation, as it is commonly done. This problem is very well known and already in Asplund et al. (2009) the proposed and possible solutions are explored, involving opacity and composition corrections, diffusion or other new mechanisms; see Asplund et al. (2009); Choi et al. (2016) and references therein for more details. In conclusion, we fix $\alpha = 1.743$ and $f_{\rm ov} = 0.032$ in all our models at it is commonly done. It can be argued that it is not assured that they are constant for all the masses and in all evolutionary phases. While it is most likely true, 3D hydrodynamic simulations or a more extensive calibration in order to relate these parameters to stellar observable properties. Regarding the chemical composition we do use the Asplund et al. (2009) abundances instead of the calibrated ones which are more consistent with the chemical evolution from the Big Bang nucleosynthesis, well aware that the $1 M_{\odot}$ models do not reproduce our Sun (neither the calibrated one does it accurately).

CHAPTER 3

The first two dredge-up events

In Chap. 1 we briefly recalled the evolution for low- and intermediate-mass stars. We refer to dredge-up events when the convective envelope is able to reach nuclear processed layers, bringing reactions products to the surface. This chapter is devoted to discuss with more details the first and second dredge-up, which is another important step before going into the third mixing event during TP-AGB; the analysis of the first two dredge-ups also serves as ground basis to compare what happens next. Numerous Kippenhahn diagrams are showed in this chapter, so here I report the legend: hatched regions (red, orange and green) refers to mixing (convection, overshoot and thermohaline); blu-ish regions, with respective colorbar, refers to burning zones. The dashed lines indicate the H-free or He-free core, if present. I will also refer to particular models with their initial mass, as it is commonly done.

3.1 The first dredge-up

At the end of the main sequence, the star develops an H-burning shell eventually with an hook feature if the hydrogen core in MS is convective (see Fig. 1.1). By means of the mirror principle, since the inert helium core contracts, the envelope must expand and the temperature decreases. Due to large opacity, the star structure becomes dominated by convection and at some point the envelope reaches the previous hydrogen core. Here the first dredge-up takes place, mixing products of H-burning. This event is shown in Fig. 3.1a and Fig. 3.2a; note how different is the ratio between the time spent before the DUP and the further evolution for the two cases. The $1M_{\odot}$ evolution before the mixing event is way slower than the one for $1.9M_{\odot}$. Indeed the $1M_{\odot}$ core still remains in complete equilibrium after TAMS, because it does not exceed the Schönberg-Chandrasekhar limit. As an order of magnitude one can consider $M_{\rm core} \lesssim 0.1M$. Since the core is still in thermal and hydrostatic equilibrium, the evolution timescale is given by the nuclear timescale $\tau_{\rm nuc}$, despite not having a nuclear energy source. When the limit is exceeded, the contraction of the core speeds up. Instead the 1.9 $M_{\odot}$ model quickly reaches the mass limit at the end of the main sequence, so that evolves way more rapidly along the subgiant

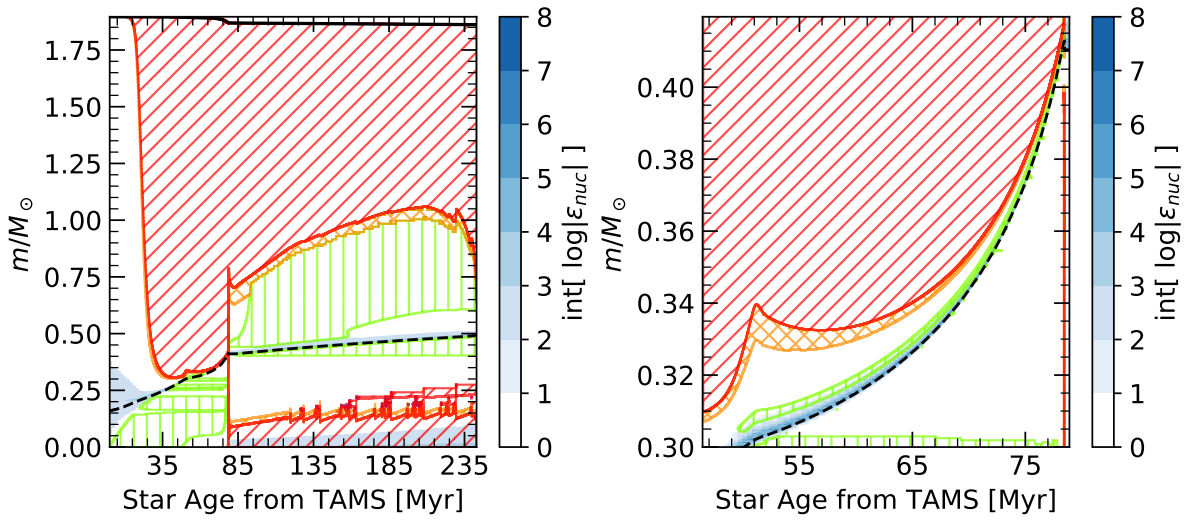

(a) Full temporal and mass range. **(b)** Zoom in the relevant region for thermohaline mixing.

Fig. 3.1: Kippenhahn diagram for a $M_i = 1.9 M_\odot$ star from TAMS to TACHeB.

branch.

Fig. 3.3 shows the evolution of the surface abundance of some hydrogen burning products. We have used the luminosity logarithm as a time proxy: it increases up to the RGB tip and then decreases, until the star settles in the quiescent core He burning phase. Note that I have not included the ^{4}He abundance in the plot; it is already the second most abundant element, $X(^4\text{He})$ increases by a relatively small fraction. Instead the plot clearly shows that ^{3}He, ^{14}N and ^{13}C mass fractions undergoes a large variation; they are respectively produced as accumulation points in the pp-chains (helium-3) and CNO cycle (the other two). We can also distinguish which models are powered by the first or the latter process of hydrogen burning: the 1 $M_\odot$ models shows large

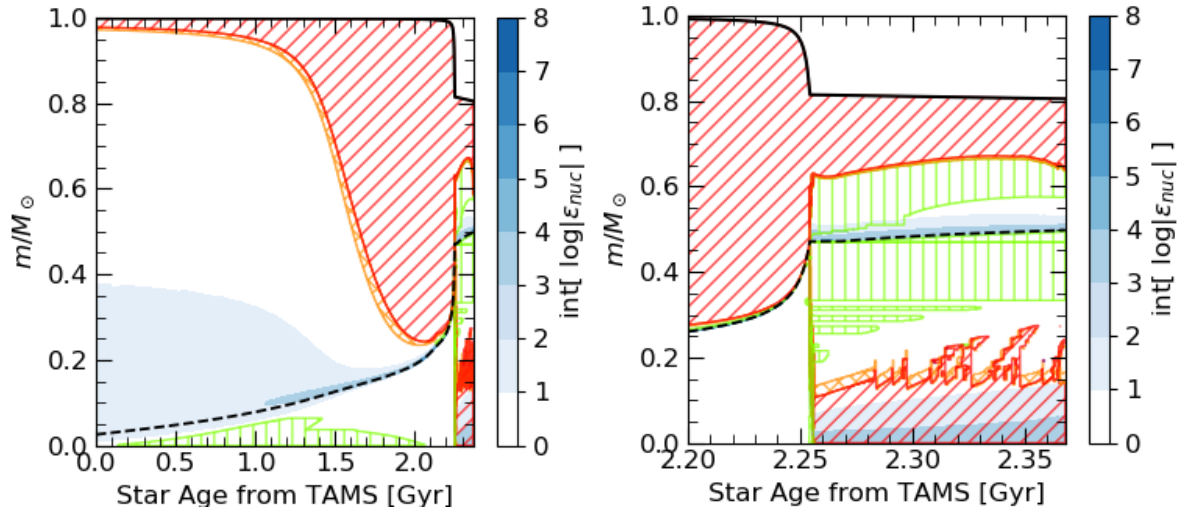

(a) Full temporal and mass range. **(b)** Zoom after the first dredge-up

Fig. 3.2: Kippenhahn diagram for a $M_i = 1 M_\odot$ star from TAMS to TACHeB. The age at TAMS is 9.06 Gyr, while the showed phase lasts about 2.37 Gyr. The He-flash takes place in a narrow time interval, where the H-burning shell is pushed outwards.

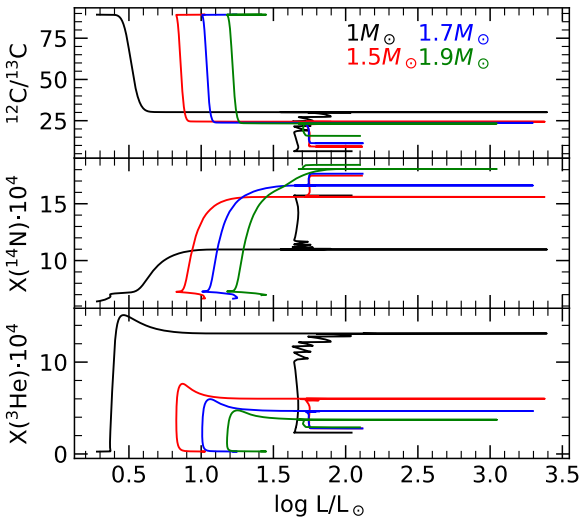

Fig. 3.3: ^{3}He, ^{14}N mass fractions and ^{12}C/^{13}C in low mass stars from TAMS to TACHeB.

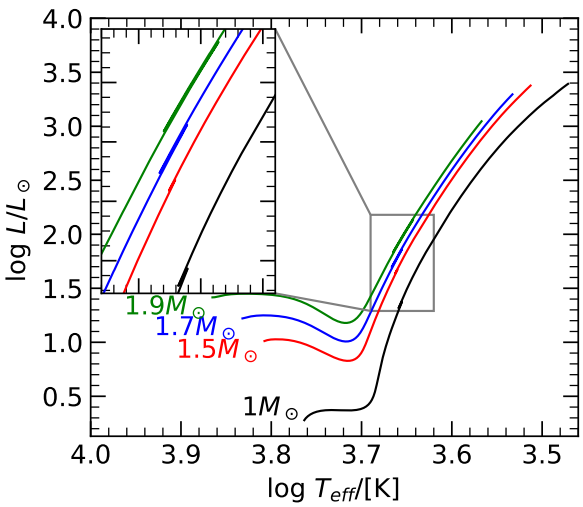

Fig. 3.4: RGB branch for four low mass stars and zoom on the luminosity bump after first dredge-up.

variation of ^{3}He abundance and limited changes of the CNO elements; in the other three cases the picture is reversed. That is because the solar-mass star runs predominantly the pp-chain while the higher masses are hot enough to efficiently burn hydrogen via CNO cycles.

However after the first dredge-up an anomalous mixing event takes place, as pointed out by Charbonnel & Zahn (2007), which cause can be found in the thermohaline mixing. The reaction ^{3}He(^{3}He,2p)^{4}He produce more particles than it started from, creating a mean molecular weight inversion if the process takes place in the external wing of the HBS. Cantiello & Langer (2010) find that low-mass stars with $M_i \lesssim 1.5$ M$_\odot$ have connected thermohaline and convection regions (so that the abundances are mixed up to the surface) just after the luminosity bump and also after the helium core ignition, and this result is derived in models with rotational mixing. However Charbonnel & Lagarde (2010) find that, when rotation is included, such threshold is not present and the thermohaline mixing affects surface abundances on the RGB in any case; they do observe the threshold in non-rotating models. On top of that, our models, which do not include rotation, shows that the thermohaline mixing is important only after He-core ignition; Fig. 3.3 clearly shows that this second mixing event takes place after the RGB tip for all masses. We can also see it in Fig. 3.1a, 3.1b and 3.2b: the thermohaline region (green) is connected to the convective envelope after the RGB tip, while they stay well separated just after the first dredge up. About the abundances, note that X(^{3}He) decreases, while the others follows the same reasoning as before. That is because in the thermoaline mixing ^{3}He works as "salt", diffuse downwards where it is burnt. As already stressed, mixing events (and eventually rotation) description still has to be improved in 1D stellar evolution codes; the discussed tension about the effects of thermohaline mixing offer another evidence. A deeper analysis is needed in order to solve this problem, but this is left for future works and it is beyond the scope of this thesis.

3.2 The second dredge-up

A second episode of mixing may take place in the high mass region of intermediate-mass stars, near the end of the E-AGB phase. The mass thresholds turns out to depend on the

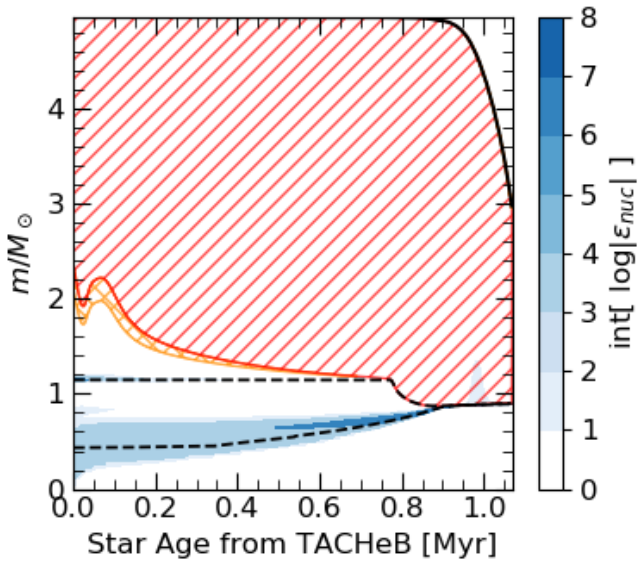

Fig. 3.5: Kippenhahn diagram for a 5 $M_\odot$ star in AGB phase

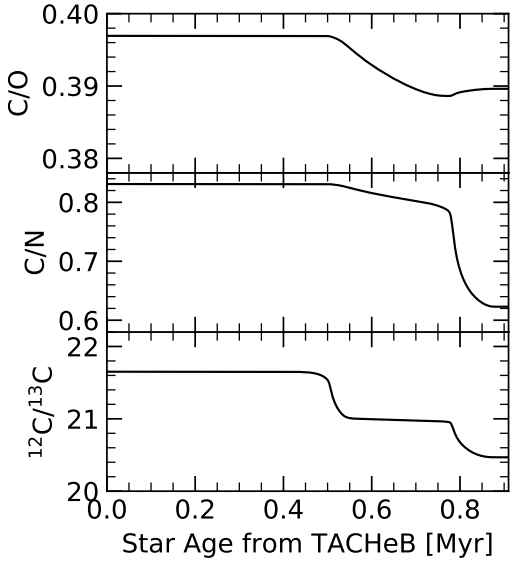

Fig. 3.6: CN, CO and $^{12}C/^{13}C$ for a 5 $M_\odot$ star during second dredge-up, in the surface.

initial composition and, not surprisingly, on the particular mixing treatment, i.e. inclusion and efficiency of overshoot. For example, we can compare Fig. 1.3 and 3.5: the second dredge-up takes place only in the second, suggesting that the limit lies somewhere between 3 and 5 $M_\odot$, as already anticipated in Sect. 1.2. It turns out that the efficency of 2DUP increases with the mass; since the event reduces the H-free core, then it directly affects the upper limit of the intermediate-mass class of stars. We can see from Fig. 3.5 that the H-free core (top dashed line) recedes from about 1.1 $M_\odot$ to 0.9 $M_\odot$, which is about 4% of the total mass variation; for higher masses we should expect even larger fraction of mixed mass, up to 1 $M_\odot$.

Similarly to 1DUP, the second dredge-up mixes hydrogen burning products with the surface

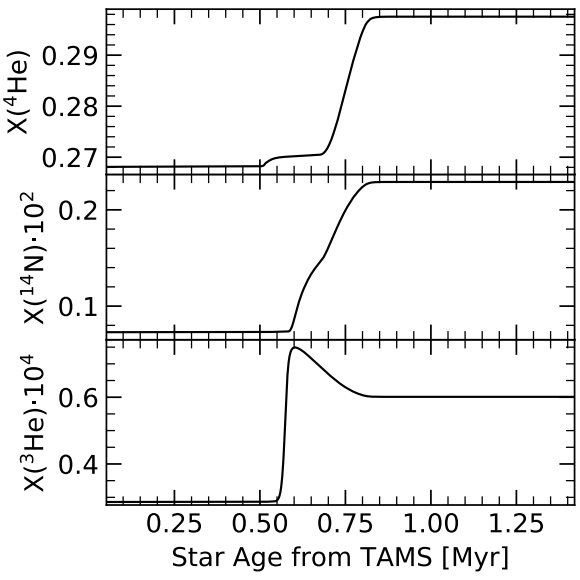

Fig. 3.7: ^{3}He, ^{4}He, and ^{14}N surface abundances for 5 $M_\odot$ star during 1DUP.

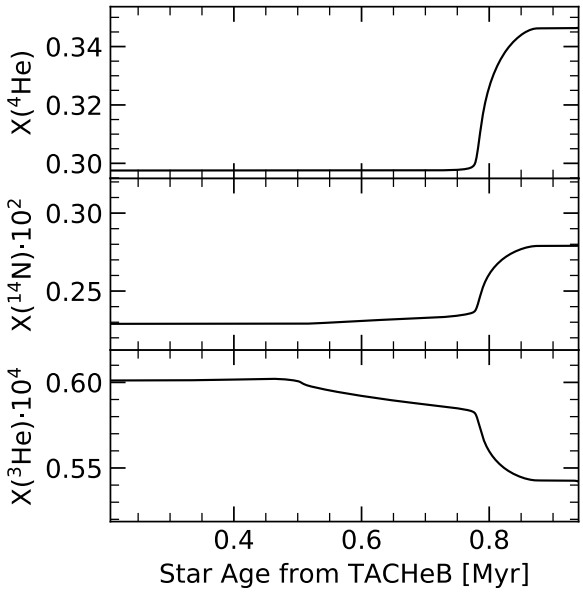

Fig. 3.8: ^{3}He, ^{4}He, and ^{14}N surface abundances for 5 $M_\odot$ star during 2DUP.

composition, but it also enters in the He rich intershell. Fig. 3.6 and 3.8 shows the variation of some element and isotopic number ratios. From both the figures it is evident that the 2DUP takes place as "two-step process": firstly, the convective envelope mixes the material from the external wing of the hydrogen burning shell; in second place the envelope involves deeper region of the intershell, and indeed the ^{4}He abundance considerably grows only in this case. It is also interesting to compare the two dredge-ups, especially Fig. 3.7 and 3.8: for the 5 $M_\odot$ the 1DUP produces slightly larger variations than the 2DUP.

CHAPTER 4

The third dredge-up

The main purpose of this thesis is to study in detail the third dredge-up, which takes place during TP-AGB phase, due to thermal instabilities of the HeBS. The present chapter is entirely dedicated at this scope; in particular we will quantify the efficiency of the 3DUP for different masses, overshoot and mass loss prescription, analyzing the consequent effects on intershell and surface composition. The legend for the Kippenhahn diagrams is the same as the previous chapter. I will refer to the computed models with their initial mass; models indicated with a *ov* subscript has been calculated with $f_{\mathrm{ov,pdcz}} = 0.008$, while the non-marked ones have no overshoot in the PDCZ. More particular cases are listed in the following.

4.1 Evolutionary details

As we already discussed in Sect. 1.2, a TP-AGB star suffers dramatic and rapid changes in the structure due to recurrent thermal pulses. I now want to discuss the main evolutionary features of a prototype $M_i = 3\ \mathrm{M}_\odot$ model, while in the next section we will see how these properties are affected when the input physics changes. First of all, the TP-AGB phase starts when the HBS is reignited again; however the meaning is that the nuclear energy generation is comparable, in order of magnitude, to the HeBS. In Fig. 4.1 this event is roughly located 6×10^5 yr before the first thermal pulse. A precise definition can be given in terms of the intershell thickness as did by Dotter (2016), which marks the onset of thermal pulses when the difference in mass of the two shells is less than 0.1 $M_\odot$.

The Kippenhahn diagram of the prototype model (Fig. 4.1) shows, qualitatively, other important features:

- The TDUP may not take place from the first pulses. Indeed for every initial mass M_i a minimum mass of the H-free core is needed to trigger the dredge-up.

- The efficiency λ is not constant even after the first event.

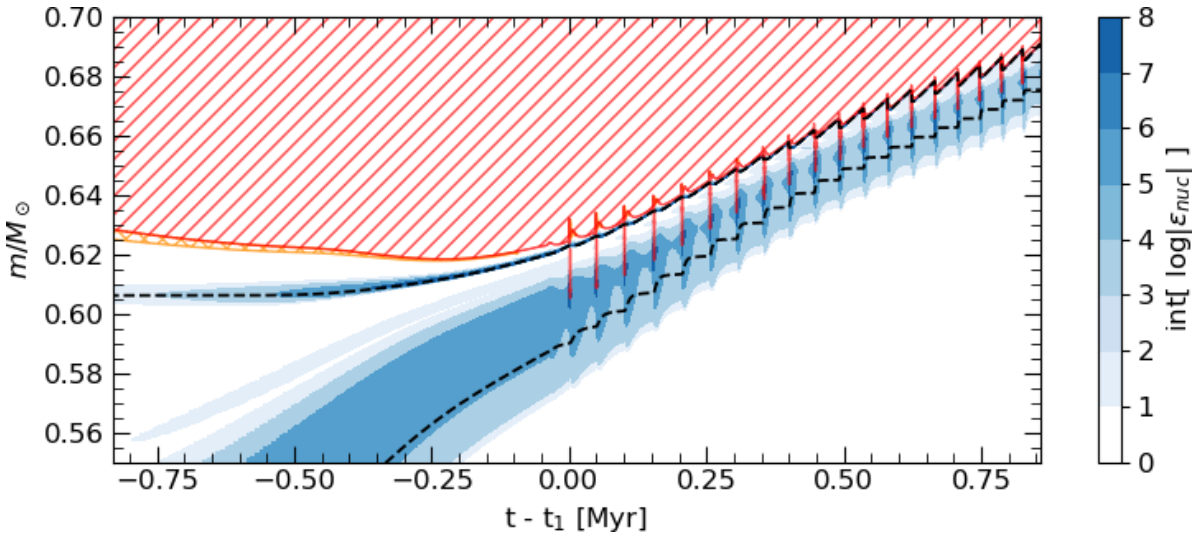

Fig. 4.1: TP-AGB phase of a $3M_{\odot}$ star. The evolution is followed up to a mass $M = 2.09\,M_{\odot}$. $t_1 = 474.985$ Myr is the star age at the first pulse. Up to that point, the model has experienced N = 19 TPs.

- Without dredge-up occurrence the growth of the H-free core is steeper. Then the white dwarf mass will be smaller.
- TP-AGB phase timescale is much shorter than previous evolutionary phases. The first TP occurs at $t_1 = 474.985$ Myr, interpulse period is $\Delta t \simeq 50000$ yr and pulses themselves are even shorter.

We can quantify these properties and even get a deeper insight by analyzing the next set of plots. The following discussion will show how the dredge-up occurence strongly affects the composition and structure evolution of TP-AGB stars. Fig. 4.3 shows the evolution of the λ parameters for our prototype, as a function of the H-free core mass M_{He}. The latter can be used as a time proxy provided that $\lambda < 1$, so that M_{He} monotonically increases. We can see that the

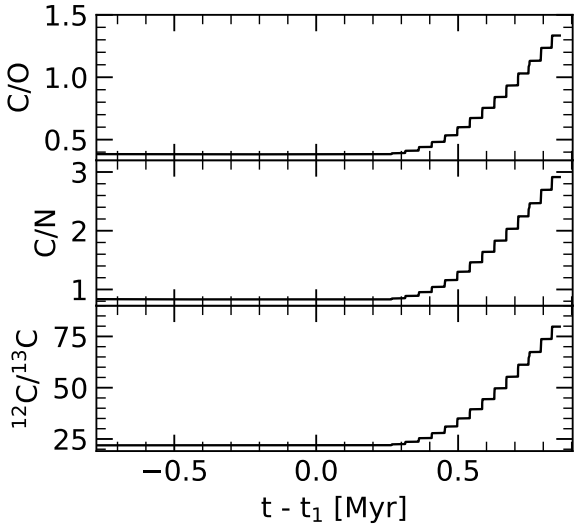

Fig. 4.2: Isotopic ratios evolution for a 3 $M_{\odot}$ TP-AGB star.

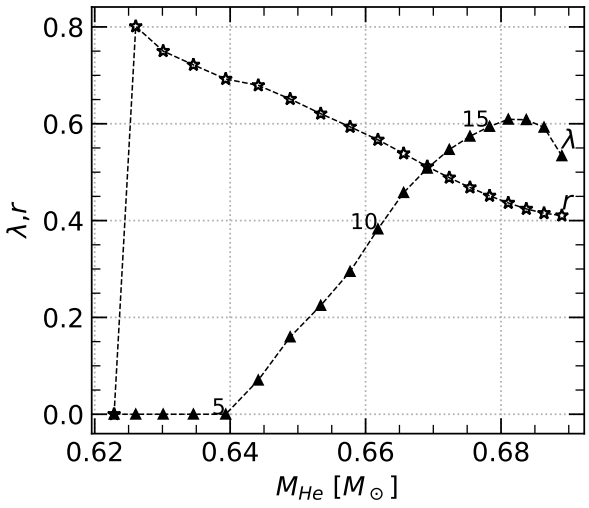

Fig. 4.3: λ and r evolution for a 3 $M_{\odot}$ TP-AGB star

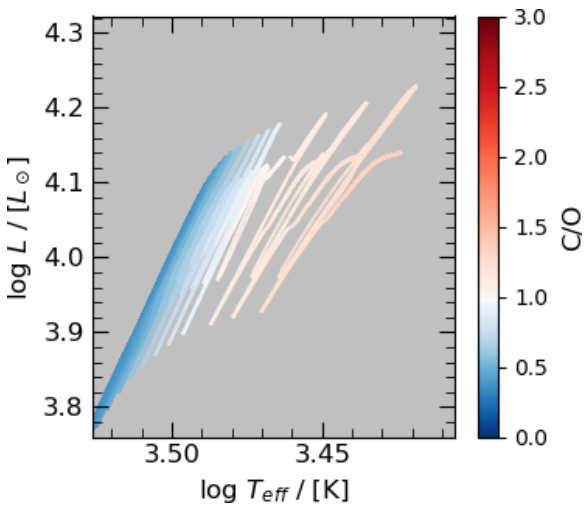

Fig. 4.4: HR diagram of TP-AGB 3M$_\odot$ star with C/O colorcoding.

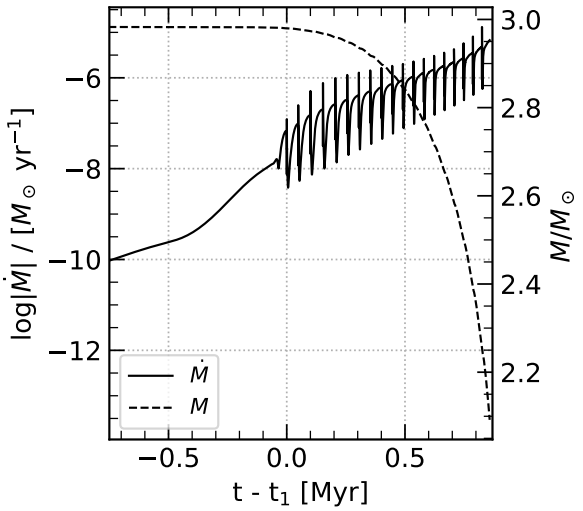

Fig. 4.5: Mass and wind evolution for TP-AGB 3M$_\odot$ star.

star experience the dredge-up from the sixth thermal pulse; the efficiency increases reaching fairly large values and then it decreases, which is a general trend (Marigo et al., 2013, see Fig. 4 and references therein). Up to now the 3DUP efficiency remains a free parameter, but many works in the literature have shown that λ depend upon total mass, metallicity, core mass (Karakas et al., 2002); however up to know a calibration is still missing, being the heavy computational cost of complete models and the uncertainties in the bare convection physics ones of the main reasons. In the following we will indeed look at the λ variation with the overshooting parameter $f_{\rm ov,pdcz}$. Besides these difficultes, the occurence of the third dredge-up strongly changes the surface composition of the star. The intershell material is brought up to the surface, in particular carbon. Fig. 4.2 shows the effect through the evolution of three isotopic ratios: it is evident that ^{12}C abundances changes the most, as expected from the typical intershell composition.

A striking example of the importance of C/O evolution is given by Fig. 4.4. As C/O < 1

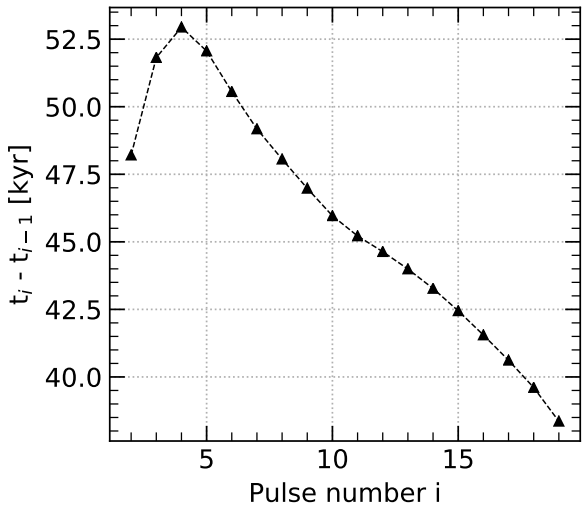

Fig. 4.6: Interpulse duration for a 3 M$_\odot$ TP-AGB star.

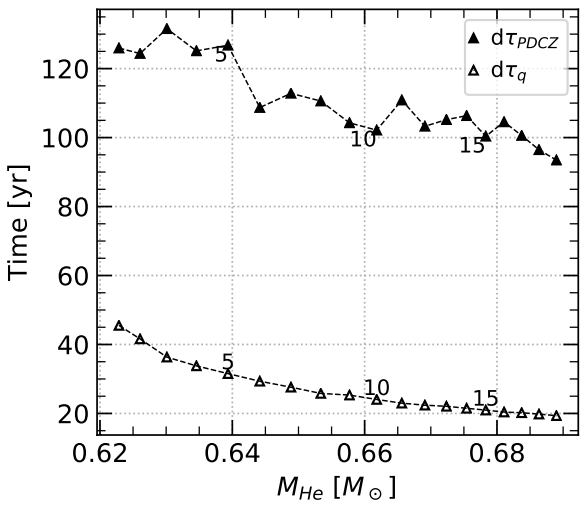

Fig. 4.7: PDCZ extinction and quenching time for a 3 M$_\odot$ TP-AGB star. See text for details.

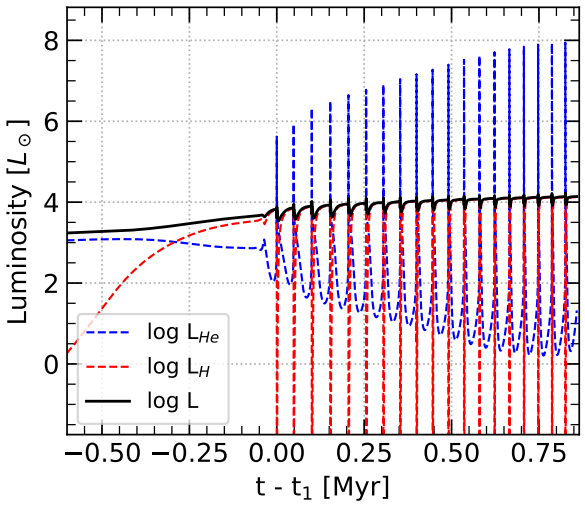

Fig. 4.8: log L, log L_H and log L_{He} for a 3 $M_\odot$ TP-AGB star.

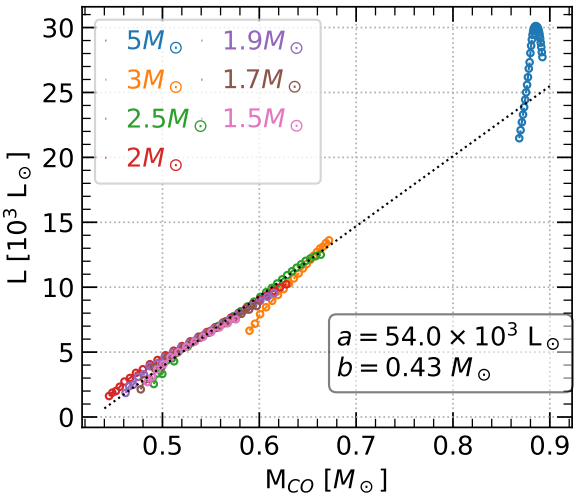

Fig. 4.9: M_{CO}-L plot for all models with $f_{ov,pdcz}$ = 0. The line fits the model with $M_i = 2.5M_\odot$, more details in Sect. 4.3.

the star slowly moves towards redder regions of HRD; as soon as C/O > 1, the star becomes C-type, opacity changes and the transition is way quicker. The composition change induced by the third dredge-up have a direct effect on the surface properties of the star; in contrast Fig. 4.5 is not directly affected by these variation, because Blöcker (1995) wind prescription has no composition dependence and it has been proposed for M-stars. The wind for C-stars should take into account the different opacity and dust composition, which point is explored in the following.

It is also interesting to quantitatively see the difference timescales involved in one pulse evolution: Fig. 4.6 and 4.7 shows, respectively, time between two pulses $\Delta t(i) = t_i$ - t_{i-1}, PDCZ duration $d\tau_{PDCZ}$ and PDCZ quenching time $d\tau_q$. The latter correspond to the time needed from the PDCZ maximum extension and its disappereance. All three quantities shows a decreasing trend, meaning that the evolution speeds up as long as the intershell becomes thinner and the core grows in mass. Furthermore the thermal pulses become more and more violent, as it is showed in Fig. 4.8; in particular the luminosity produced by helium burning increases with time, triggering a larger expansion of the outer envelope. Indeed all of the energy releases in the flash is used to increase the stellar radius, as it is evident from Fig. 4.8.

A key aspect of investigations about TP-AGB stars is represented by the core mass-luminosity relations: Paczyński (1970) first noted that the quiescent luminosity, namely during the interpulse, is tightly related to the size in mass of the core of these stars. These correlations are important both for interpretation of observational data, because they link surface properties, and for synthetic calculations of stellar models. The CMLRs are divided into: (i) classical linear relation like:

$$L(M_{CO}) = a(M_{CO} - b) \tag{4.1}$$

which can be derived from homology relations and assuming certain conditions described in Tuchman et al. (1983); (ii) technical relations that fully take into account further dependencies besides M_{CO}, i.e. composition, full amplitude regime, large efficiency of 3DUP. A comprehensive discussion about the validity of these relations is given by Marigo et al. (1999). Fig. 4.9 purpose is to qualitatively motivate such relations; however the plot also shows where some

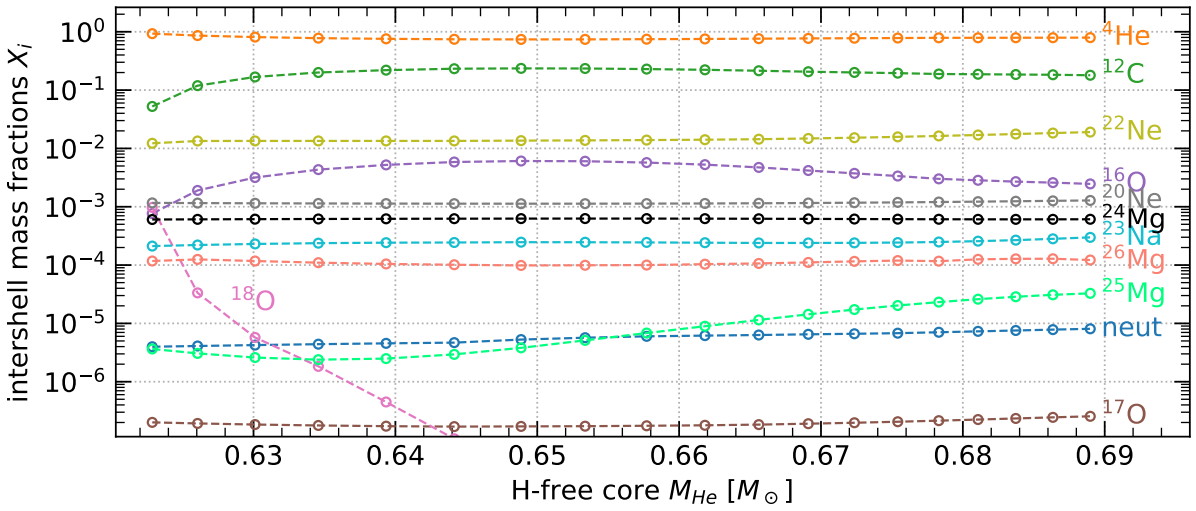

Fig. 4.10: Intershell abundances of a $3M_\odot$ TP-AGB star. They are estimated just after PDCZ is extinguished but before the 3DUP occurs, in inert region. This means that they represent the composition of the dredge-upped material. ^{13}C is not present because its abundance is found several order of magnitude below the others.

issues are. The first pulses are systematically found at lower luminosities from what predicted by the linear trend; in this case one of the Tuchman et al. (1983) conditions is not fulfilled, namely requiring that the whole surface luminosity is provided by a burning shell. In the first pulses the contraction of the H-free core still gives a non negligible contribution to the surface luminosity.

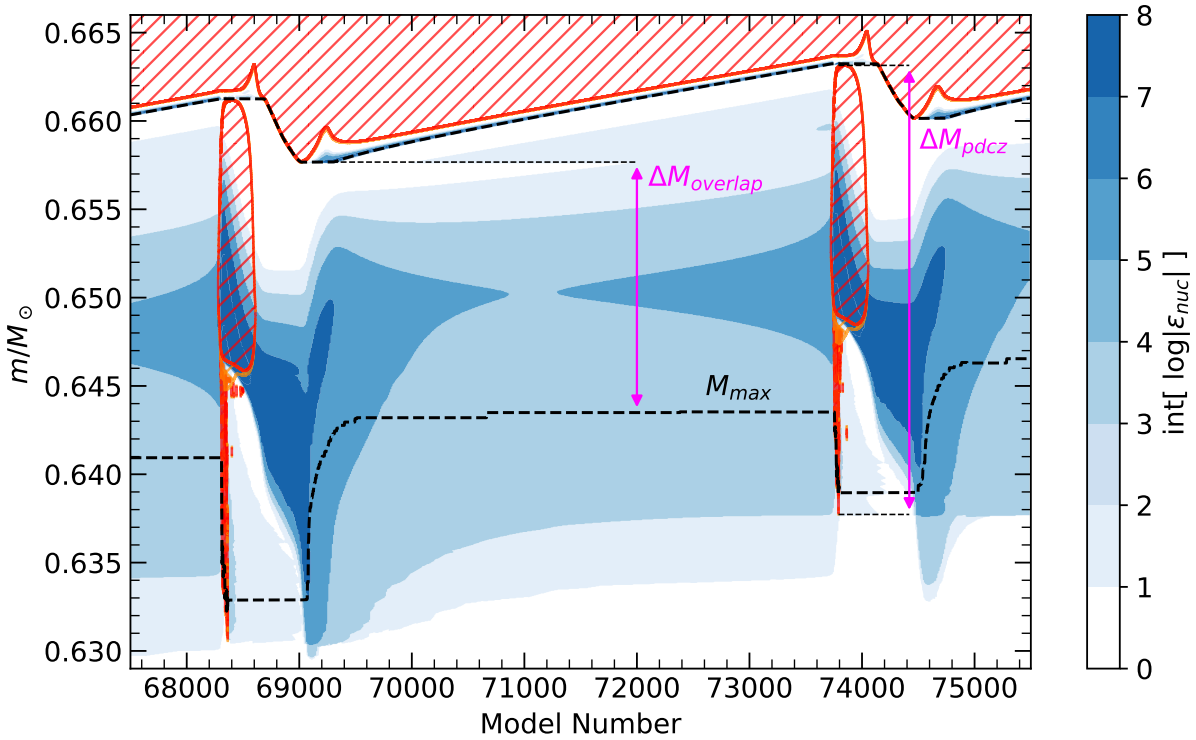

Fig. 4.11: 14th and 15th pulses for a 3M$_\odot$ star with $f_{ov,pdcz}$ = 0.008. Here I mark again the quantities needed to calculate r; note that when overshooting in PDCZ boundaries is active, the intuitive definition of r does not change despite the visual one does.

Fig. 4.10 shows the composition of intershell material just after each pulse, a part of which eventually reaches the surface due to 3DUP. After the last (calculated) TP the intershell is mainly composed by $\sim$ 79% ^{4}He, $\sim$ 17.9% ^{12}C, $\sim$ 1.9% ^{22}Ne and the rest by the other elements. The comparison of the intershell abundances with observation is a way to infer the value of $f_{\rm ov,pdcz}$, as we will discuss in the following. Fig. 4.10 also shows that neutrons are produced in AGB stars; this is a known result (Herwig, 2005, see for a review). We are not including the s-process in the models because the input nuclear network is limited at ^{26}Al, but it is beyond the scope of this work in any case. Finally we can observe that the abundances are consistently varying when r is changing more rapidly (Fig. 4.3). In the last TPs where r variation is limited, almost all X_i have reached a constant value.

Lastly I want to anticipate the effect of setting $f_{\rm ov,pdcz} > 0$ by comparing the Kippenhahn diagrams in Fig. 1.4 and 4.11. Activating the overshooting around PDCZ around the mixing of CO core material in the intershell, which is eventually enriched by ^{12}C and ^{16}O. Consequently the following dredge-up brings up to the surface material richer in carbon and oxygen. I want also to note that, a careful comparison between the two cases would reveal that $\lambda(f_{\rm ov,pdcz} = 0) > \lambda(f_{\rm ov,pdcz} = 0.008)$ for the 15$^{\rm th}$ TP. At first glance the result can sound counter-intuitive, however the analysis of previous pulses already gives an explaination. I defer a deep discussion about it for Sect. 4.3, but in the case of Fig. 4.11 the first event of third dredge-up occurs at earlier pulses and the 15$^{\rm th}$ pulse takes place when the 3DUP efficiency is already decreasing.

4.2 Convective overshooting at PDCZ boundaries

In this section I will explore different values of the overshooting parameter $f_{\rm ov,pdcz}$, fixing everything else. In particular the initial mass is set to $M_i = 2.5$ M$_\odot$ and the other convective boundaries are not modified. It is important to note that the models showed in this section have $C = 1$; however none of them has been able to completely lose the hydrogenic envelope, reaching the post-AGB phase without diverging. Nevertheless the calculation stopped at the

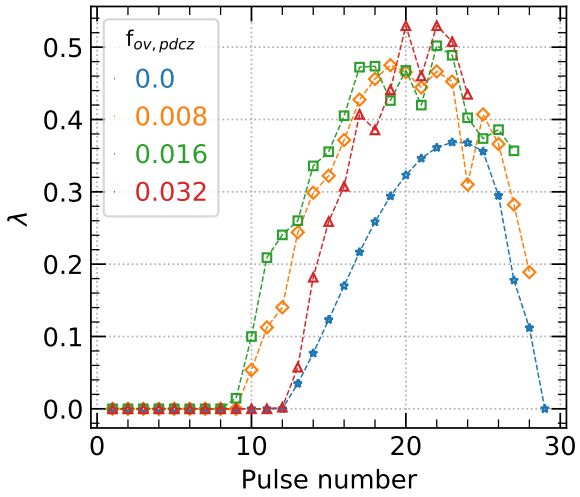

Fig. 4.12: λ for different PDCZ overshooting prescripion for 2.5M$_\odot$ star, as a function of pulse number.

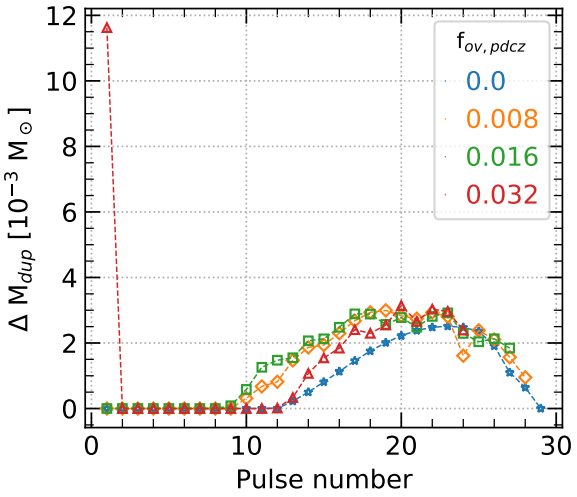

Fig. 4.13: ΔM$_{\rm dup}$ for different PDCZ overshooting prescription for 2.5M$_\odot$ star, as a function of pulse number.

last pulses, which are the most violent and the structure is cold, because $\log\left|\dot{M}_{\rm B}\right| \simeq 4-5$. A number near to 25-30 pulses has been computed for each $f_{\rm ov,pdcz}$ value, then we are still able to draw some conclusions out of the grid of models. The explored overshooting parameters are $f_{\rm ov,pdcz} = 0, 0.008, 0.016, 0.032$, to which I refer as Fi with $i = 0, 1, 2, 3$ respectively. Herwig (2000, hereinafter H00) did a similar analysis and it is our main reference point for the following discussion.

The first interesting point to discuss is how the 3DUP efficiency is affected by the overshooting in the pulse-driven convection zone boundaries. Fig. 4.12 shows the λ evolution along the pulses for every value of $f_{\rm ov,pdcz}$. All four models present the same evolutionary trend but the overall efficiency is different. As predicted by H00, λ increases if $f_{\rm ov,pdcz} \neq 0$; more interestingly the maximum is roughly equal for the three non-zero values of the same parameter. The same applies to the start of the decaying trend, which takes place at lower TP number compared to the no-overshooting case. It is also expected that the first event of mixing occurs at earlier pulses, since PDCZ overshoot seems to help the 3DUP efficiency. Fig. 4.12 shows that this is indeed true for $F1$ and $F2$, but the $F3$ model starts to dredge-up at the $11^{\rm th}$ as $F0$. A possible explaination is found in Fig. 4.13: $F3$ model suffer a super-efficient dredge-up at the first TP, but $\lambda = 0$ because the efficiency is defined by comparing the i-th and (i+1)-th thermal pulses. This event decreases the core mass and consequently the following pulses are slightly weaker compared to $F0$, $F1$ and $F2$.

The obtained result seems in contrast with the result of H00 (see his Fig. 13): he founds that for the $9^{\rm th}$ thermal pulse of a 3 $M_\odot$ star λ is strongly correlated to the overshoot on the bottom of PDCZ. However we have fully computed all tracks with a fixed value of $f_{\rm ov}$ for the respective convective border as specified in Sect. 2.2.3, while in H00 the value was being changed after PDCZ extinction of the $8^{\rm th}$ TP. The conditions are systematically different, which makes difficult to compare with. In order to illustrate this point, H00 model has the same $M_{\rm H}$ at $9^{\rm th}$ TP; the four models here instead does not have equal $M_{\rm H}$ for the i-th thermal pulse, after 3DUP is activated, since the previous evolution is not the same. This is illustrated in Fig. 4.14; all cases but $F3$

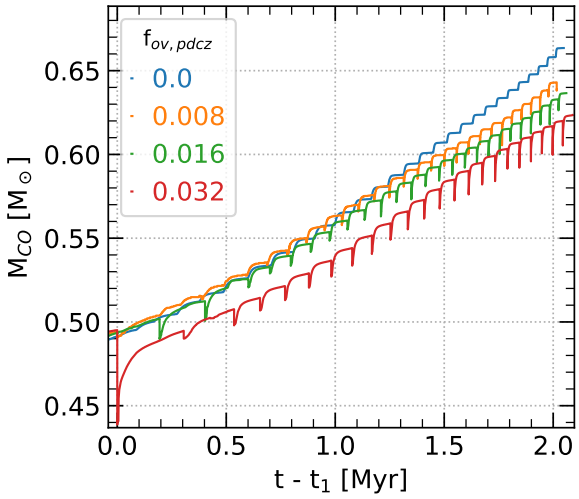

Fig. 4.14: $M_{\rm CO}$ evolution of a 2.5$M_\odot$ TP-AGB star for different $f_{\rm ov,pdcz}$, as a function of time since first pulse.

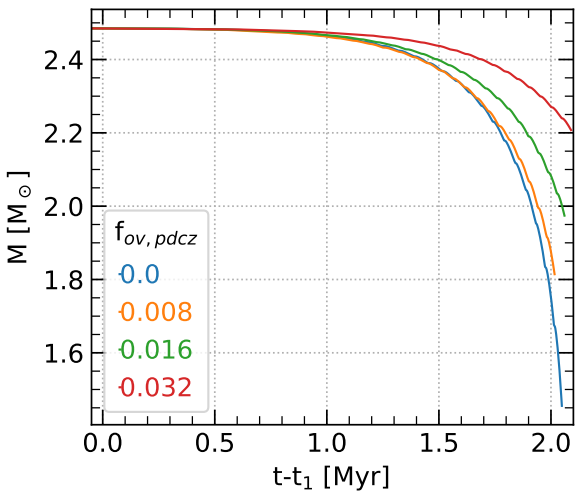

Fig. 4.15: Total mass time evolution for $F0$, $F1$, $F2$ and $F3$ only during the TP-AGB phase. The mass at t_1 is $M = 2.485 M_\odot$.

(due to DUP on the first TP) have roughly the same M_{CO} until 3DUP is activated; then the three curves separate. The core mass of $F0$ model grows the most since the 3DUP is the less efficient, while $F1$ and $F2$ separation is less pronounced because of the different $f_{ov,pdcz}$. A larger $f_{ov,pdcz}$ implies that the PDCZ is larger in mass and reaches deeper regions of the CO core, which then shows a less steep growth. The point which we just made has also profound implications in the structure of the star as a whole. In fact, even if the (Blöcker, 1995) wind is not directly dependent on the composition, it is affected anyway by the different $f_{ov,pdcz}$. The link is due to the core mass-luminosity relation: varying the core mass changes the surface luminosity during interpulses, also where the star spends most of its time. Since $\dot{M}_B \propto L^{3.1}$ (Eq. (2.9)), a larger core mass implies a stronger wind. The consequent anti-correlation between the total mass and the core mass is visually represented in Fig. 4.14 and 4.15: the order of the models is inverted between the two figures.

In Fig. 4.16 r is plotted as a function of the pulse number for the four models. We found that the degree of overlap is not strongly dependent on $f_{ov,pdcz}$, even if there is a decreasing trend for larger overshooting parameter. All four models present the same evolutionary trend with $r \simeq 0.4$ as absolute minimum. The result is in contrast with the trend found by Marigo et al. (2013), where the sole presence of 3DUP makes r rapidly drop very close to zero. This should be investigated more deeply and it may constitute matter of future works comparing complete and hybrid stellar evolution codes. The cause of discrepancy may be explored among the different input physics, numerical resolution for which I looked for a compromise between quality of models and execution time.

We can know translate what we did so far, namely how the pulse anatomy depends on $f_{ov,pdcz}$, to study the evolution of chemical composition for both the surface and intershell. They are tightly correlated by the third dredge-up and the magnitude of the PDCZ overshooting. The effects of 3DUP on the surface composition are highlighted in the element and isotopic ratios. C/O is the most relevant and its evolution is plotted in Fig. 4.17: all four model show the signature step trend. As soon as the dredge-up takes place, convective bubbles rapidly bring up

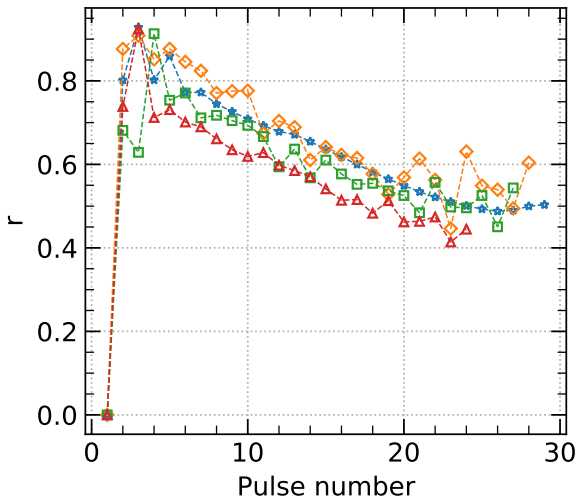

Fig. 4.16: Overlap degree r of a 2.5$M_\odot$ TP-AGB star for different $f_{ov,pdcz}$ as a function of pulse number. The color legend is reported in Fig. 4.17.

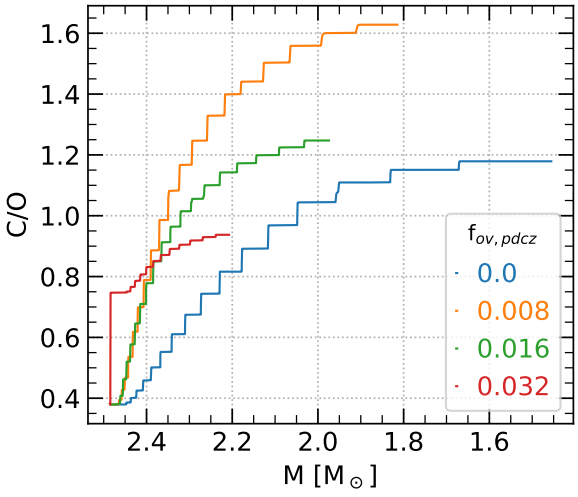

Fig. 4.17: Surface C/O through TP-AGB for different $f_{ov,pdcz}$ values. The total mass is used as a time proxy.

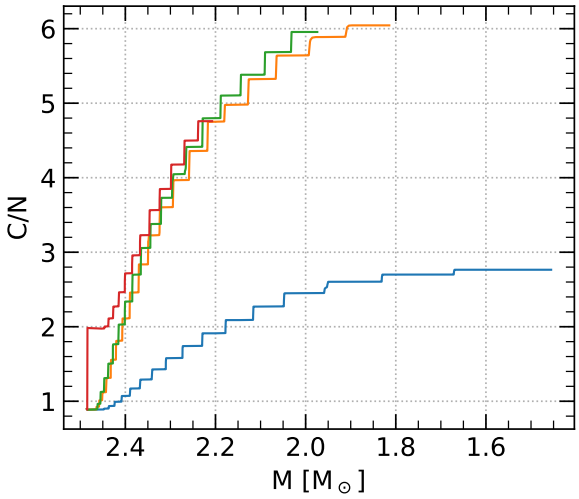

Fig. 4.18: Surface C/N through TP-AGB for different $f_{\rm ov,pdcz}$ values. The color legend is reported in Fig 4.17.

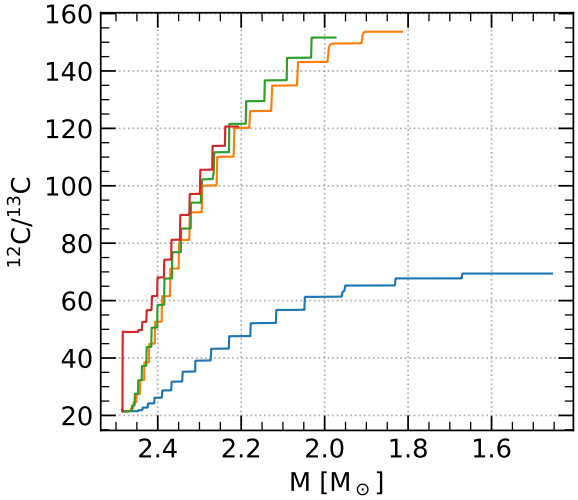

Fig. 4.19: Surface carbon isotopic ratio through TP-AGB for different $f_{\rm ov,pdcz}$ values. The color legend is reported in Fig 4.17.

the material. It is useful to take constant-mass (time) slices after the occurrence of the firsts DUPs, namely for $M \gtrsim 2.35 M_{\odot}$. Then the C/O ratios are in this order: $F1 > F2 > F3 > F0$. The hierarchy is not trivial but the explanation is found in the delicate equilibrium between the amount of C and O in the dredge-upped material: taking $F0$ as a reference case, $F1$ develops a larger carbon-to-oxygen ratio because $\Delta M_{\rm dup}$ is larger and the PDCZ deepening into CO core is limited. The latter point is indeed the reason why $F2 < F1$: since $f_{\rm ov,pdcz}$ is larger and $\Delta M_{\rm dup}$ is very similar, the dredge-upped material is more oxygen rich in the $F2$ model than $F1$. The moved material is even richer in ^{16}O for $F3$, which may develop a final C/O even smaller than $F0$ case if the evolution is carried further. The explanation is even more established by the next set of plots. Figs. 4.18 and 4.19 shows the carbon-to-nitrogen and carbon isotopic ratios, which of course do not depend on oxygen. We can indeed see that all three models with $f_{\rm ov,pdcz}$

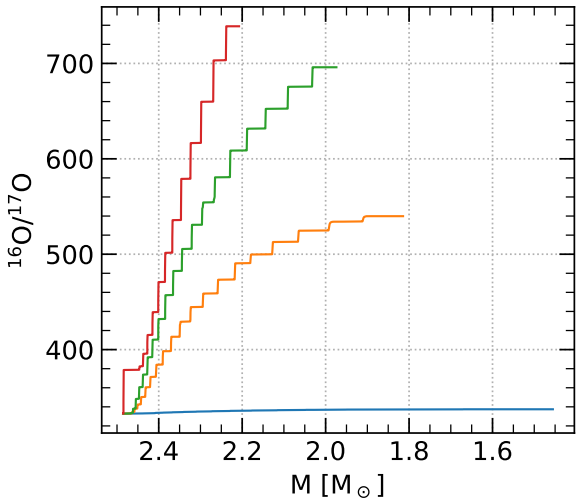

Fig. 4.20: Surface ^{16}O/^{17}O through TP-AGB for different $f_{\rm ov,pdcz}$ values. The color legend is reported in Fig 4.17.

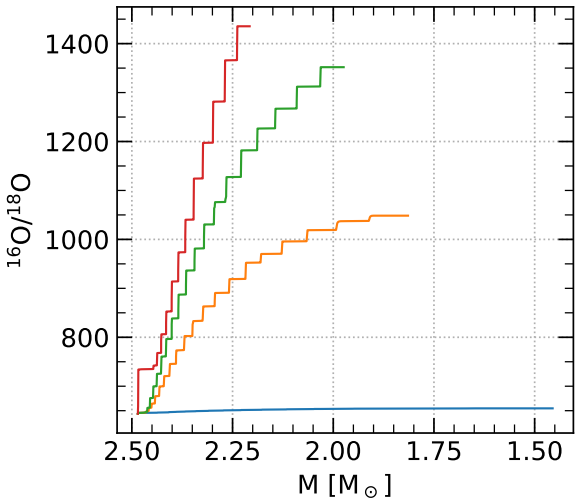

Fig. 4.21: Surface ^{16}O/^{18}O through TP-AGB for different $f_{\rm ov,pdcz}$ values. The color legend is reported in Fig 4.17.

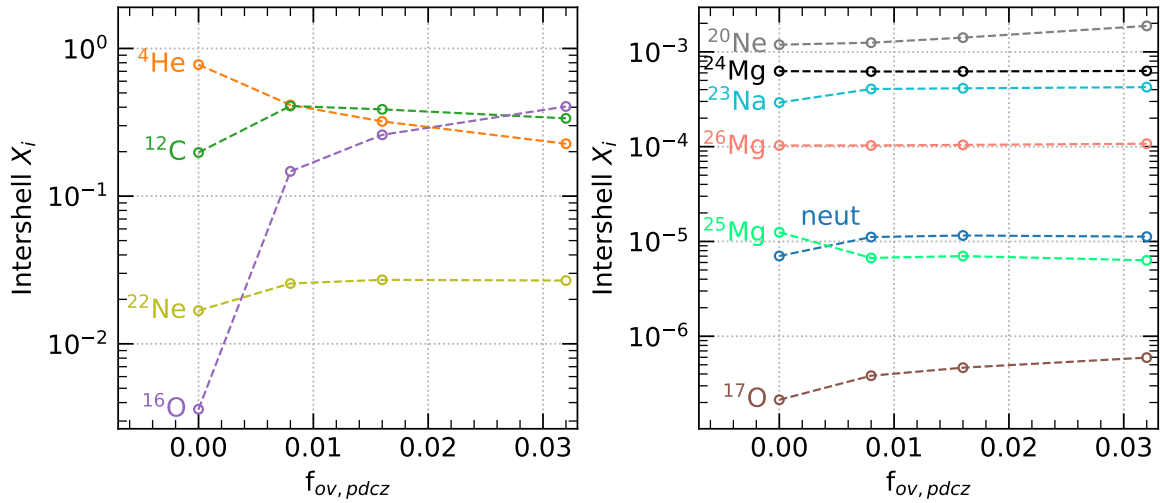

(a) Four most abundant elements

(b) Less abundant elements.

Fig. 4.22: Intershell abundances at 24$^{\text{th}}$ TP for different values of $f_{\text{ov,pdcz}}$.

develop higher values of both ratios, and that is due just to the larger ΔM_{dup} than $F0$ case and because in the connection with the CO core is also adding more ^{12}C. However the plots establish that C/N and ^{12}C/^{13}C do not depend on $f_{\text{ov,pdcz}}$ magnitude as much as C/O does. Finally, in the last two graphs the two oxygen isotopic ratios are plotted, respectively Fig. 4.20 and 4.21. Here again we find a strong sensitivity to the magnitude of overshooting in PDCZ boundaries. For $F0$ model both ratios stay almost constant, while the steepness of the other three curves is correlated to $f_{\text{ov,pdcz}}$, producing higher final ratios since they start from the same composition. The correlation is indeed justified because the larger is $f_{\text{ov,pdcz}}$, the larger is the mass of CO core (mainly made by ^{12}C and ^{16}O) involved in the mixing. These strong correlation can be used to constrain the additional mixing from observational data, e.g. Kamath et al. (2012).

The previous discussion involving surface abundances is clearly valid for TP-AGB stars which still retain a (even small) fraction of their hydrogenic envelope. However another diagnostic is offered directly by intershell abundances, if compared with hydrogen-deficient post-AGB stars. The prototype of this class, which gives the name to the entire group, is PG 1159. These star suffered a very late thermal pulse and exposed the intershell material. Herwig (2000) showed indeed that is possible to constrain the overshooting parameter at the bottom boundary[1] of PDCZ by comparing the intershell abundances with observational data of PG 1159 and WC-type of central stars of planetary nebulae. The result of that investigation has given the range $0.01 \lesssim f_{\text{ov,pdcz}} \lesssim 0.03$, but later it has been updated to $0.005 \lesssim f_{\text{ov,pdcz}} \lesssim 0.015$ (Herwig, 2005). A more recent work by Wagstaff et al. (2020) gives a similar interval with $f_{\text{ov,pdcz}} = 0.008$ being the most promising value. Fig. 4.22 shows the intershell abundance of labeled elements just passed the 24$^{\text{th}}$ thermal pulse, from the models calculated for this thesis. That specific pulse has been chosen because it is the last one of $F3$ model; in addition r is already flattened for all four cases, meaning that the abundances have reached stationarity and are close to their final value. We can observe that not all elements have the same sensibility on the $f_{\text{ov,pdcz}}$ value.

[1] I want to clarify this point. Actually we set the same $f_{\text{ov,pdcz}}$ on all PDCZ boundaries, bottom and top. As it is qualitatively clear from Fig. 4.11 and as found by Herwig (2000) the overshooting on the top boundary is irrelevant, so it is customary to discuss about the bottom boundary.

As expected ^{16}O is the most dependent on the PDCZ overshooting: it sharply increases for $0 \lesssim f_{\mathrm{ov,pdcz}} \lesssim 0.008$ and the curve becomes less steep for greater values. Despite being less evident, the same increasing or decreasing trend applies to the other elements, but ^{12}C. The latter reach its maximum for $F1$ model; this is consistent with the previous discussion about surface element and isotopic ratios. The material of CO core in any case adds carbon (in absolute terms) to the intershell, but the mixed mass is still oxygen-rich. The delicate equilibrium breaks down in favor of ^{16}O when $f_{\mathrm{ov,pdcz}} \gtrsim 0.008$, and after all the fraction of carbon gently decreases. Precisely the additional ^{12}C at disposal allows to produce more ^{14}N with the CNO cycle during the interpulse, which is left behind by the advancing HBS; in the next thermal pulse ^{14}N is destroyed to burn alpha particles $^{14}\mathrm{N}(\alpha,\gamma)^{18}\mathrm{F}(\beta^{+}\nu)^{18}\mathrm{O}(\alpha,\gamma)^{22}\mathrm{Ne}$. That is able to explain the

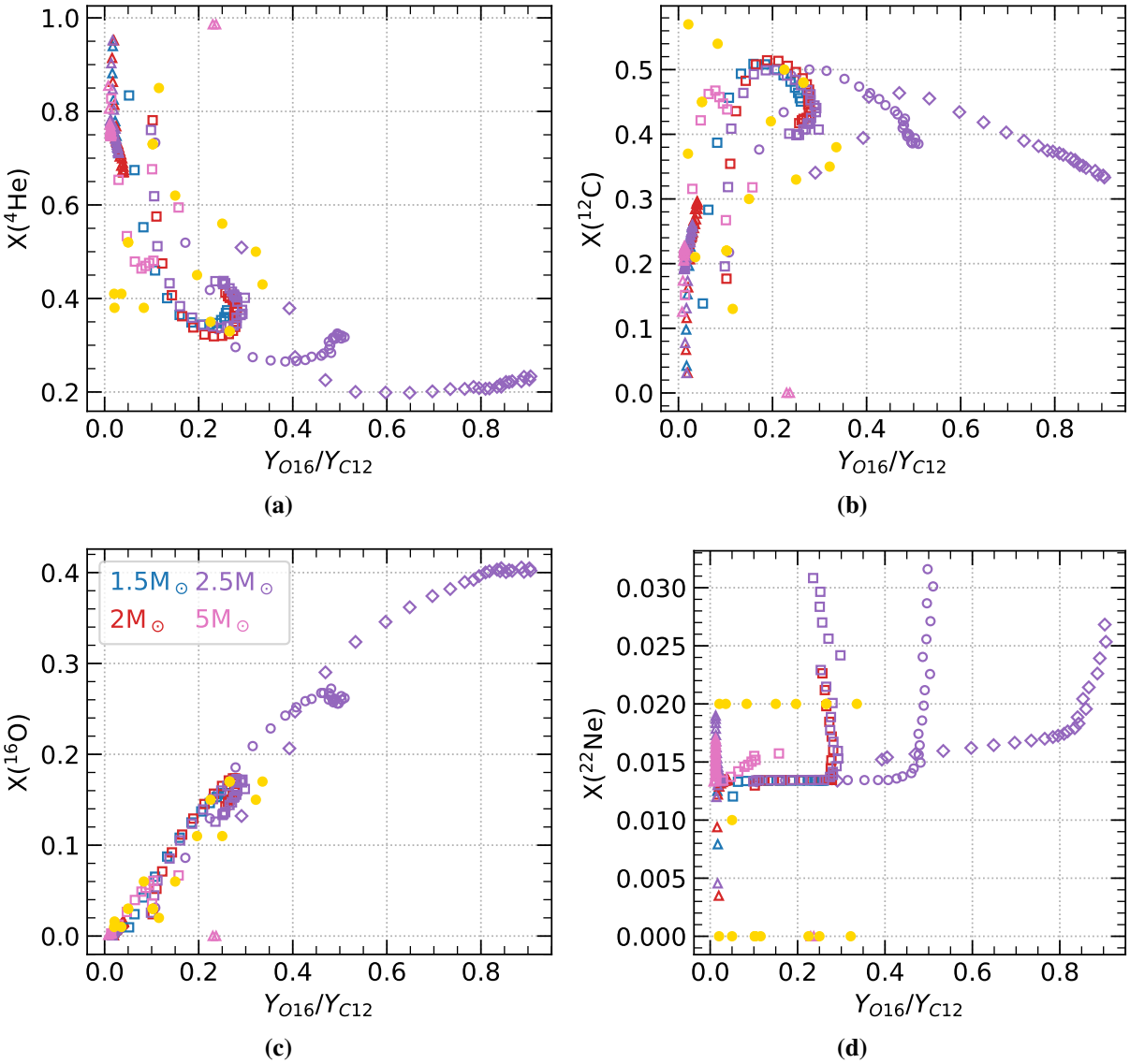

Fig. 4.23: Intershell abundances for PG 1159 stars, [WC] central stars of planetary nebula and for some selected models. Gold circles indicates observational data (see Tab. 4.1). For the predicted abundances, masses are distinguished by color (c) and $f_{\mathrm{ov,pdcz}}$ by empty marker. Respectively $f_{\mathrm{ov,pdcz}} = 0, 0.008, 0.016, 0.032$ are indicated by triangle, square, circle and diamond. More details in the text.

enhanced production for larger $f_{\mathrm{ov,pdcz}}$ of ^{22}Ne, which also acts as a seed for proton capture into ^{23}Na. Another reaction of the CNO cycle is responsible for the $X(^{17}\mathrm{O})$-$f_{\mathrm{ov,pdcz}}$ correlation, combined with the increased ^{16}O abundance; that is $^{16}\mathrm{O}(p,\gamma)^{17}\mathrm{F}(\beta^{+}\nu)^{17}\mathrm{O}$. With the intershell richer in ^{16}O is it also possible to synthetize a larger quantity of ^{20}Ne directly with α-captures.

The drawn results seem in agreement with the physical intuition, so that we can now compare them to the observational data. Fig. 4.23 shows the surface abundances of PG 1159 stars and [WC]-type central stars of planetary nebulae and the intershell abundances, for every pulse, of four selected models. The models with $M_i \neq 2.5M_{\odot}$ are described in more details in Sect. 4.3. Before actually comparing the observations with the theoretical prediction, it is interesting to note how the abundances evolve for the single models. For fixed value of $f_{\mathrm{ov,pdcz}}$, the tracks initially suffer sensible variation of the abundances; in the end they reach their asymptotic values and condense in a narrow region of the plane, which is roughly the same indipendently on the initial mass. Note that the ending region of the tracks is found at larger $Y_{\mathrm{O16}}/Y_{\mathrm{C12}}$ for increasing $f_{\mathrm{ov,pdcz}}$. In addition, for the no-overshooting case the oxygen-to-carbon number ratio remains almost constant. The observed data span the lower half part of the x-axis, never exceeding $Y_{\mathrm{O16}}/Y_{\mathrm{C12}} = 0.35$. That already rules out most of the points belonging to the $f_{\mathrm{ov,pdcz}} = 0.016, 0.032$ classes. These models have also too little ^{4}He fraction and they are too rich in oxygen and neon. Instead the value $f_{\mathrm{ov,pdcz}} = 0.008$ seems to reproduce quite well the

Object	Mass fractions				References
	He	C	O	Ne	
PG1707+427	0.52	0.45	0.03	0.0	Werner et al. (2015)
PG1159-035	0.33	0.48	0.17	0.02	Jahn et al. (2007)
PG2131-066	0.73	0.22	0.03	0.0	Werner & Rauch (2014)
PG0122-200	0.73	0.22	0.03	0.0	Werner & Rauch (2014)
PG1424-535	0.52	0.45	0.03	0.01	Werner et al. (2015)
PG1144+005	0.38	0.57	0.016	0.02	Werner et al. (2016)
PG1520+525	0.43	0.38	0.17	0.02	Werner et al. (2016)
MCT0130+1937	0.73	0.22	0.03	0.0	Werner & Rauch (2014)
HS0704+6153	0.56	0.33	0.11	0.0	Dreizler et al. (1994)
HS1517+7403	0.85	0.13	0.02	0.0	Werner & Herwig (2006)
[WC] Abell-78	0.35	0.5	0.15	0.0	Koesterke & Werner (1998)
[WCE] NGC1501	0.5	0.35	0.15	0.0	Werner & Herwig (2006)
RXJ12117.1+3412	0.38	0.54	0.06	0.02	Werner et al. (2005)
NGC246	0.62	0.3	0.06	0.02	Werner et al. (2005)
K1-16	0.33	0.48	0.17	0.02	Werner et al. (2005)
HS2324+397	0.41	0.37	0.01	0.0	Werner et al. (2005)
Longmore4	0.45	0.42	0.11	0.02	Werner et al. (2005)
NGC7094	0.41	0.21	0.01	0.02	Werner et al. (2005)

Tab. 4.1: PG1159 stars and [WC]-type central stars of planetary nebulae surface abundances with respective reference.

observed pattern; that is proven in particular in Fig. 4.23c, where the experimental points are less spreaded on the plane and assume a well-defined trend. The worst agreement is found for $X(^{22}\mathrm{Ne})$; surely there is room of improvement of the models, however the neon abundance are still poorly known: out of all objects they assume three values $X(^{22}\mathrm{Ne}) = 0, 0.01, 0.02$. The bottom-line of the discussion is that additional mixing around PDCZ is needed, since $f_{\mathrm{ov,pdcz}} = 0$ cannot reproduce the observations. However the most promising value is $f_{\mathrm{ov,pdcz}} = 0$, which also confirms the result found by Wagstaff et al. (2020). We can also retrieve suggestions for future work: the $0 \lesssim f_{\mathrm{ov,pdcz}} \lesssim 0.008$ should be spanned more accurately, but also metallicity effect have to be investigated.

4.3 The effect of overshooting on different initial masses

After finding the best-fit value for the overshooting parameter $f_{\mathrm{ov,pdcz}}$ it is worth to compare all the calculated models with the found value and the no-overshooting case. The main purpose it to extend the previous discussion made among the four value for the overshooting parameter. Here is the list of the two classes: (i) the $f_{\mathrm{ov,pdcz}}$ case has been calculated for $M_i = 1, 1.5, 1.6, 1.7, 1.9, 2, 2.5, 3, 5 M_\odot$, that will be indicated in the text with the initial mass and a subscript *ov*, i.e. $3_{\mathrm{ov}}\ M_\odot$; (ii) the no-overshooting models have the same initial masses but $M_i = 1.6 M_\odot$, and they are indicated as before without the subscript. In total we have 17 models, some of them already have been showed in Fig. 4.23.

Before entering the details of this section main matter, I want to briefly present some of

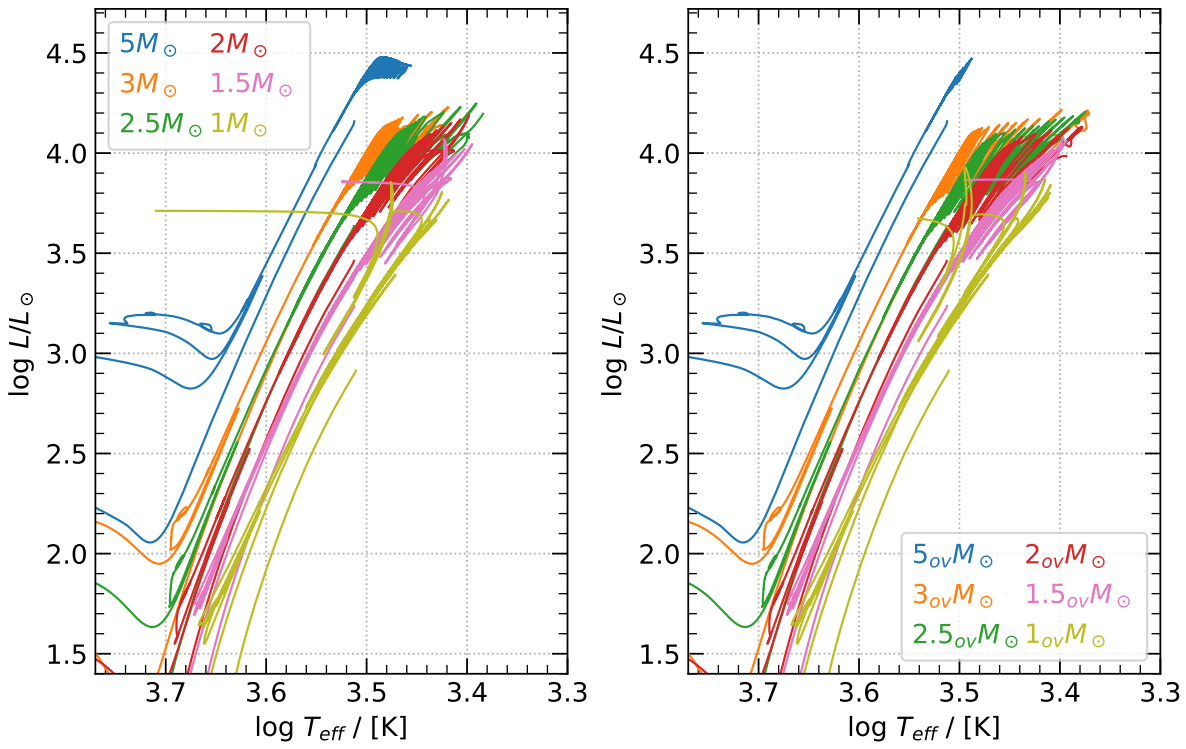

(a) $f_{\mathrm{ov,pdcz}} = 0$ **(b)** $f_{\mathrm{ov,pdcz}} = 0.008$

Fig. 4.24: HR diagram for selected models with different initial masses, focused in their brightest and coolest part. The core He-burning and TP-AGB phases (eventually until divergence) are fully included.

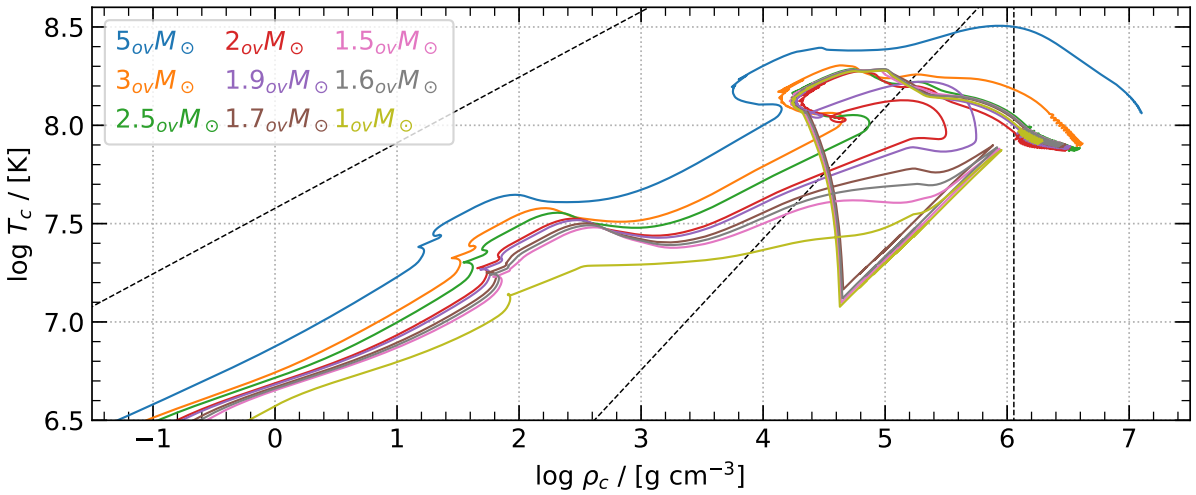

Fig. 4.25: T_c-ρ_c diagram for all initial masses up to TP-AGB phase. The dashed lines are useful to guide the eye across regions of radiation, ideal gas and degeneracy gas. Their definition can be found in Kippenhahn & Weigert (1990, Sect. 16.2)

the full tracks from the grid of models. It has to be noted that for $M_i > 1.6M_\odot$ the tracks encountered divergence before completing TP-AGB. Different meshing and timestep solutions have been explored; the divergence is encountered during the drop of $L_{\rm He}$ after a TP and the star is expanding. It occurs almost always when the structure has low $T_{\rm eff}$. Typically the code stop the calculation when $\dot{M}$ has reached large values of $10^{-4} - 10^{-5}$ $M_\odot$ yr^{-1}; we are able to compute a sufficient number of thermal pulses up to this point, where the tracks diverge during one of the final TPs. Fig. 4.24 shows selected evolutionary tracks in the temperature-luminosity plane for both classes. We can see that `MESA` is able to go through the full He-flash phase; this is another delicate phase and the second most time-consuming point of the evolution. The position in the HR diagram during TP-AGB phase is affected by the value $f_{\rm ov,pdcz}$. That is caused by the different evolution of C/O (see Fig. 4.17): for $f_{\rm ov,pdcz}$ a larger number of pulses are condensed in a narrow $T_{\rm eff}$. Instead if C/O grows faster, the enhanced separation in effective temperature between pulses begins before. Fig. 4.25 shows all the tracks for the $f_{\rm ov,pdcz} = 0.008$ class in the $T_c - \rho_c$ plane. Here we are able to see which stars experience the He-flash from the shape of the track. The occurrence of the main flash leads the adiabatic expansion of the core, which cools down. The following flashes, much less violent, heats up the core setting up the star in the quiescent core He burning (Paxton et al., 2011). This characteristic ν-shape is traced by the models with $M_i \leq 1.7M_\odot$. The core of $1.9M_\odot$ and $2M_\odot$ eventually becomes mildly degenerate, but that is not enough to trigger a nuclear runaway. Then we can give an estimate for mass separation between the low- and intermediate-mass classes; that is somewhere between $1.7M_\odot$ and $1.9M_\odot$, rather than $2M_\odot$ as indicated before in Sect. 1.1.

Following a similar logic as before, we start the discussion with the characteristic parameters of the third dredge-up, λ and r. Fig 4.26 show the efficiency parameter as a function of the thermal pulse number, respectively for the $f_{\rm ov,pdcz} = 0$ and 0.008 case. In the plots only the models for which the dredge-up occurs are included: the minimum initial mass to experience the 3DUP is $1.9^{+0.0}_{-0.2}M_\odot$ for the no-overshooting case; the error bars are naively assigned observing that for $M_i > 1.9M_\odot$ the 3DUP does take place, while the first models lower in mass is $1.7M_\odot$.

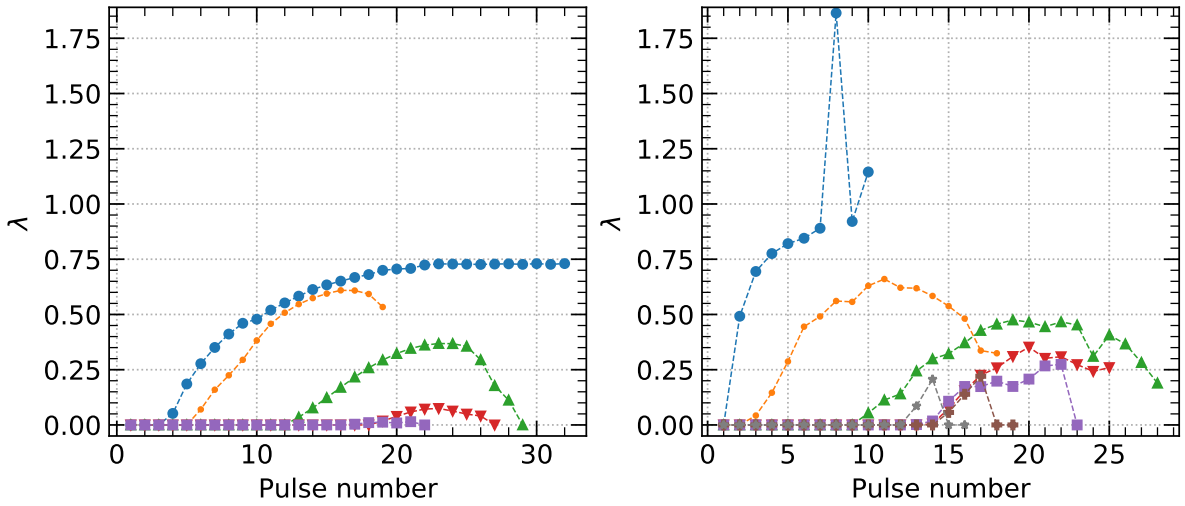

(a) $f_{\mathrm{ov,pdcz}} = 0$. The color legend is in Fig. 4.27a. **(b)** $f_{\mathrm{ov,pdcz}} = 0.008$. The color legend is in Fig. 4.27b.

Fig. 4.26: λ for all calculated models which experience the third dredge-up.

However λ for $1.9M_{\odot}$ is limited below 1.5%, namely the dredge-up is extremely inefficient. For this reason the "true" lower limit is near to $M_i = 1.9M_{\odot}$ rather than $M_i = 1.7M_{\odot}$. When the additional mixing is activated the minimum mass drops to $1.6^{+0.0}_{-0.1}M_{\odot}$, where the error bars are assigned following the same logic. Concerning instead the time evolution, in general the occurrence of overshooting around PDCZ enhance the efficiency of the third dredge-up. Interestingly the effect is less and less pronounced going from the $1.6_{\mathrm{ov}}M_{\odot}$ to $3_{\mathrm{ov}}M_{\odot}$ where λ reaches almost the same maximum. The $5_{\mathrm{ov}}M_{\odot}$ case shows again an increase in λ. That is another point which needs and it is worth to study in even more details, in order to understand if it a numerical artifact or not. A possible approach may be to refine the grid of models near $3_{\mathrm{ov}}M_{\odot}$ and increasing the spatial resolution, from which the third dredge-up is hardly dependent (see Sect. 4.4). However this approach anti-correlates directly with the time needed to compute the models, as it is common among the complete stellar evolution codes.

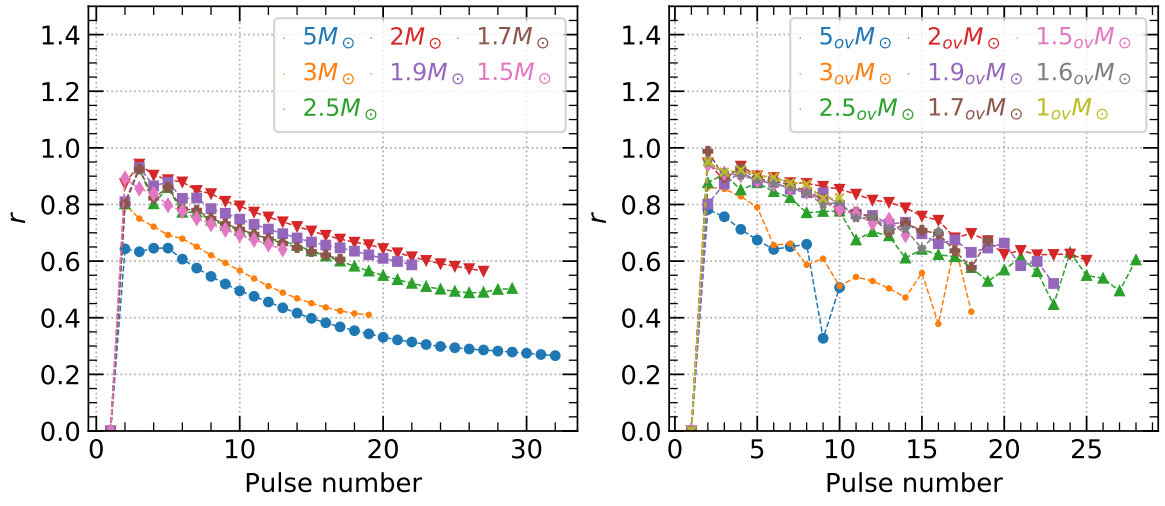

(a) $f_{\mathrm{ov,pdcz}} = 0$ **(b)** $f_{\mathrm{ov,pdcz}} = 0.008$

Fig. 4.27: Degree of overlap r for all initial masses of the grid.

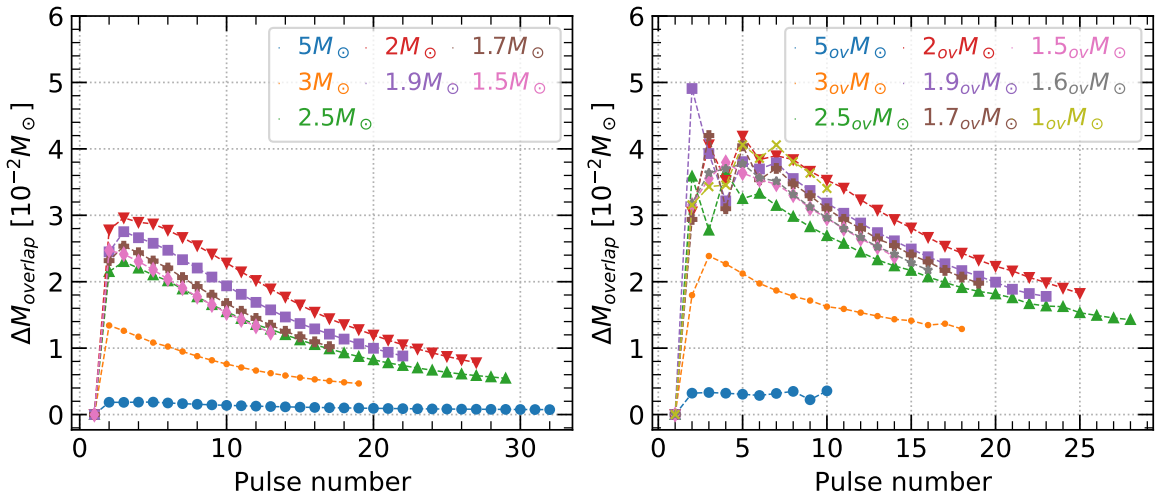

(a) $f_{\text{ov,pdcz}} = 0$ **(b)** $f_{\text{ov,pdcz}} = 0.008$

Fig. 4.28: $\Delta M_{\text{overlap}}$ evolution as a function of pulse number.

The evolution of degree of overlap r is plotted in Fig. 4.27a for the non-overshooting models and Fig. 4.27b for $f_{\text{ov,pdcz}} = 0.008$. As found in the previous Sect. 4.2, r remains roughly the same between the two cases. That is because, even if the PDCZ penetrates in the CO core and the dredge-up is in general more efficient, $\Delta M_{\text{overlap}}$ increases because the PDCZ is also wider in mass. That is quantitatively showed in Fig.s 4.28a and 4.28b. For both overshooting prescriptions r and $\Delta M_{\text{overlap}}$ are found to increase from $1M_\odot$ to $2M_\odot$, for which almost the full curve is above the others. Then, the two quantities decreases for $M_i \gtrsim 2M_\odot$, reaching an absolute minimum for $5M_\odot$. This hierarchy also reflects to the thickness of the intershell region, since it is of the same order as $\Delta M_{\text{overlap}}$.

Fig. 4.29 plots the minimum mass of the CO core $M_{\text{CO,min}}$ able to trigger the 3DUP as a function of the initial mass of the models. That is defined as the M_{CO} just before the first thermal pulse interested by the third dredge-up. As we can see the inclusion of overshooting in the PDCZ boundaries systematically lowers $M_{\text{CO,min}}$, but it does not affects equally all initial masses. The effect is more pronounced for low mass stars and the discrepancy between the two trends becomes thinner for intermediate mass stars; in the higher mass model the difference is even negligible if compared to the others. Marigo et al. (2013) Fig. 4 compares the $M_{\text{CO,min}} - M_i$ trend for several authors. We do find a similar shape and the same absolute minimum for $2M_\odot$ as Weiss & Ferguson (2009), but our version just adds more heterogeneity to the sea of results. That is common occurrence when calculating these quantities, e.g. λ, which strongly depends by the input physics, a still insufficient knowledge of convection and mixing and numerical technicalities. This full work is slowly converging to the need of a careful and precise calibration of characteristic parameters of TP-AGB phase with observations.

Lastly about this section, I want to mention the core mass-luminosity relations possible sensitivity to the overshooting around PDCZ. Here we are considering Fig.s 4.9 and 4.30. The dotted line is a fit for $2.5M_\odot$ model in the full-amplitude regime; the parameters are given according to Eq. (4.1). I want to point out that the fit has been included both to show qualitatively that such relations are motivated and to have a reference curve to make a visual comparison between $f_{\text{ov,pdcz}} = 0, 0.008$, rather than an attempt to find a new core mass-luminosity relation.

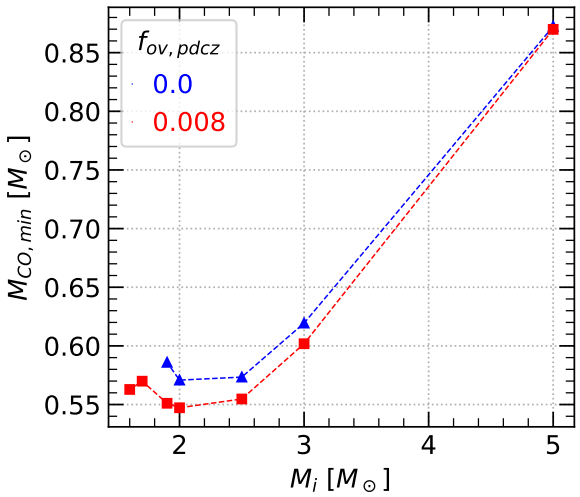

Fig. 4.29: Minimum core mass to trigger 3DUP as a function of M_i.

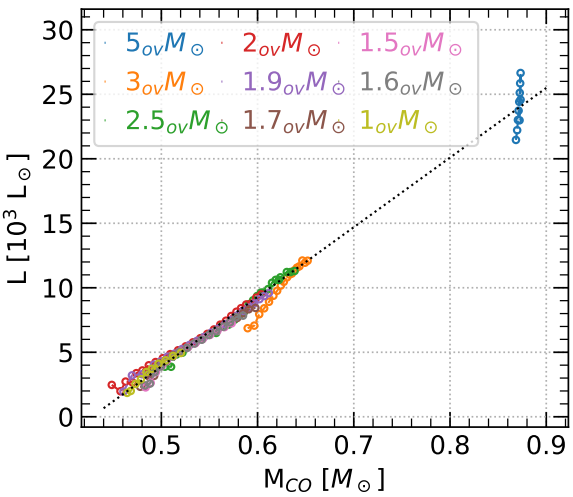

Fig. 4.30: M_{CO}-L plot for all *ov* models. The fit is the same as in Fig. 4.9.

We can notice that there is not an appreciable tilt or offset due to $f_{ov,pdcz}$ variation, even if it changes how the CO core grows in time. The $5M_\odot$ and $5_{ov}M_\odot$ models are both out of the classical linear trend, which is a known fact due to occurrence of hot bottom burning and it violates one of the assumptions of Tuchman et al. (1983). The bottom-line is that additional overshooting around PDCZ does not affects strongly the linear trend suggested by the no-overshooting case; minor adjustment may be included due to the (current) composition dependence of CMLR, since the variation of $f_{ov,pdcz}$ modifies the evolution of chemical abundances of the surface (Marigo et al., 1999, § 2.2)

4.4 Changing the mass loss prescription

Mass loss plays an important role in the evolution of AGB stars. An appropriate description is crucial for modeling these object. Even modest changes in the $\dot{M}$ can considerably affect the evolution of that late stages: it determines how long the AGB phase lasts and consequently the mass range and the initial-final mass relation for white dwarfs; the mass loss rate also influences the contribution of AGB stars in the integrated light and their dust content evolution. Given its relevance, its implementation in stellar evolution codes is critical in order to make reasonable predictions. Actually it is widely believed that radiation pressure on dust and pulsation drive the stellar wind from these type of star. A recent review about this argument is given by Höfner & Olofsson (2018). This wind mechanism depends dramatically on the dust composition; that is formed by gas condensation eventually lifted by pulsations, then it reflects the surface abundances of the star. The type of dust and molecules forming in the atmosphere is determined by the amount of oxygen or carbon not locked in the CO molecule; oxygen-rich atmosphere of M-stars are able to form Mg/Fe-silicate dust grains, i.e. quartz, olivine. On the opposite C-stars are dominated by carbonaceous dust grains as graphite or amorphous carbon. In particular the second is thought to be the one driving the dusty wind (Bladh et al., 2019, and references therein). A critical parameter for this wind mechanism is the carbon excess, defined when C/O > 1 as:

$$\mathrm{C} - \mathrm{O} = \log\left(Y_\mathrm{C} - Y_\mathrm{O}\right) - \log\left(Y_\mathrm{H}\right) + 12 \tag{4.2}$$

The different opacity sources suggests that a proper mass loss prescription should take into account the star's composition. We have indeed seen that a star can become carbon rich during the TP-AGB phase thanks to the third dredge-up. The models I presented so far all utilize Blöcker (1995) prescription for the whole evolution. That is appropriate for O-rich stars and eventually it does not take into account the transition from C/O < 1 to C/O > 1.

In this section we will head towards a more appropriate description for the mass loss mechanism. Recent works (Pastorelli et al., 2019; Marigo et al., 2020, references therein) are describing the AGB mass loss as two-stage process: a pre-dust mass loss stage and a dust-driven (pulsation-assisted) mass loss. The first is motivated by the unsuitable environment present in the early phases. Here the star has still relatively low luminosity and the wind is thought to be driven by Alfvén waves (Cranmer & Saar, 2011). Later the star's atmosphere becomes cool enough and the gas can condense into dust particles. The material is eventually lifted by pulsations and pushed away by the radiation pressure. For simplicity, in this section I skip the first stage, focusing on the second. The following mass loss routine (`FORTRAN` based) has been implemented in `MESA` using the so-called `other_wind` hook inside `run_star_extras.f` file: (i) for the O-rich phase I still use Blöcker (1995) recipe, with the parameter explained in Sect. 2.2; (ii) for C/O > 1 regime I used the results of the radiation-hydrodynamic simulation (RHD) of carbon-rich atmospheres cured by Mattsson et al. (2010); Eriksson et al. (2014); Bladh et al. (2019). Their models requires suitable conditions for the carbon dust-driven wind even after C/O > 1, translating in a minimum value of the carbon excess $(\text{C-O})_{\text{min}}$. That also depends on the specific stellar parameters, as luminosity, mass and effective temperature. It turns out that in the early carbon-rich phases, where C-O, T_{eff} and L/M are small, the RHD routine produces zero or very low values for $\dot{M}$. That is physically interpreted as the need of stellar wind to be driven by pulsations alone (Marigo et al., 2020). To sum up, the mass loss is chosen as:

$$\dot{M} = \begin{cases} \dot{M}_{\text{B}} & \text{for C - O} < 7.90 \\ \begin{cases} \dot{M}_{\text{pulsation}} \text{ or } \dot{M}_{\text{B}} & \text{if } \dot{M}_{\text{dust}} < 10^{-15} M_{\odot}\ \text{yr}^{-1} \\ \dot{M}_{\text{dust}} & \text{otherwise} \end{cases} & \text{for C - O} \geq 7.90 \end{cases} \tag{4.3}$$

where $\dot{M}_{\text{dust}}$ is given by the RHD routine and so it is the threshold C - O = 7.90. Such limit corresponds to $(\text{C/O})_{\text{min}} \simeq 1.11 - 1.12$, slightly depending on the current hydrogen abundance. After entering that regime, if the RHD routine returns zero or small values $\dot{M}_{\text{pulsation}}$ or Blöcker (1995) is used. The recipe for the pulsation-driven wind is given by Marigo et al. (2020):

$$\dot{M}_{\text{pulsation}} = \exp\left(a \left(\frac{M}{M_{\odot}}\right)^{b} \left(\frac{R}{R_{\odot}}\right)^{c}\right) \qquad a = -789,\ b = 0.558,\ c = -0.676 \tag{4.4}$$

The grid of models for the present section is visually represented in Fig. 4.31. It consists of five tracks, with initial mass and mass loss prescription marked in each subplot. The size of the set is limited because the routine is still on a phase of initial testing inside `MESA`. That step is fundamental for possible future developments of the research, but we are still able to draw interesting results. The tracks has been constructed by inserting the mass loss routine in the models $2.5_{\text{ov}} M_{\odot}$ or $2_{\text{ov}} M_{\odot}$ (see Sect. 4.2 and 4.3) before reaching C/O > 1. That corresponds to

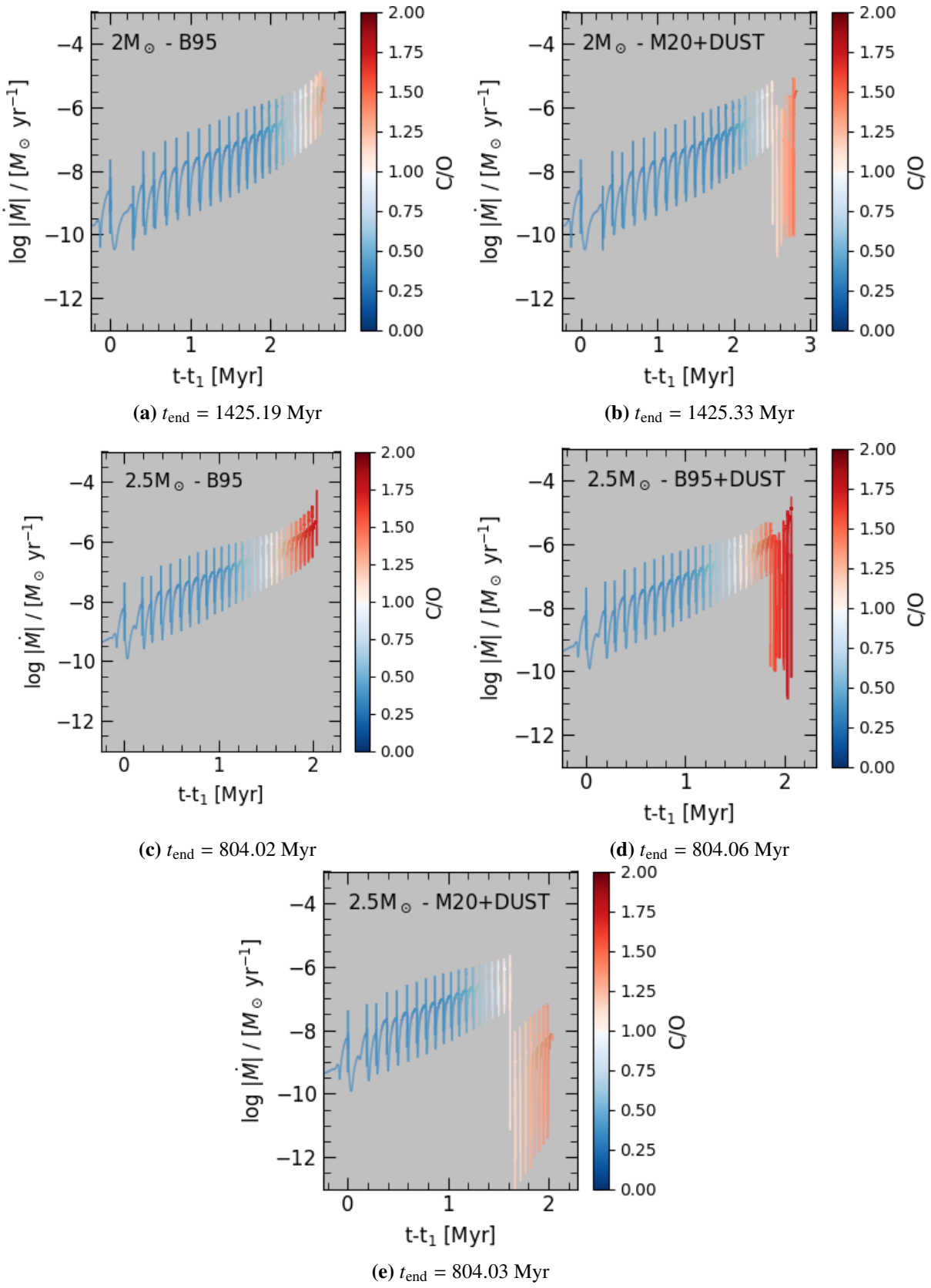

(a) $t_{\rm end}$ = 1425.19 Myr

(b) $t_{\rm end}$ = 1425.33 Myr

(c) $t_{\rm end}$ = 804.02 Myr

(d) $t_{\rm end}$ = 804.06 Myr

(e) $t_{\rm end}$ = 804.03 Myr

Fig. 4.31: $\log|\dot{M}|$ evolution as a function of time for different wind prescriptions. The label in the plot report M_i and the wind prescription used for C-O > 7.90. `B95` = (Blöcker, 1995), `M20` = (Marigo et al., 2020), `DUST` = RHD simulations. To be clear, `B95+DUST` means that Blöcker (1995) recipe has been used when the RHD routine returned zero or small values. $t_{\rm end}$ is the star age at the divergence point.

exploiting $2.5_{\rm ov}M_\odot$ and $2_{\rm ov}M_\odot$ up to just after the 18$^{\rm th}$ and 22$^{\rm nd}$ TP, respectively. Note also that the base model $2.5_{\rm ov}M_\odot$ has been computed with $C = 1$, while all its extensions used $C = 1/2$. Instead $2_{\rm ov}M_\odot$ is computed entirely with $C = 1/2$.

The set of plots in Fig. 4.31 shows the $\dot{M}$ evolution from the occurrence of the first thermal pulse. The C/O colorbar guides the eye in the transition between the two regimes described in Eq. (4.4). For the two `M20+DUST` models we see a sharp drop as soon as $\dot{M}_{\rm pulsation}$ sets in. That is because pulsation(only)-driven wind produces low mass loss rates; the slower evolution effectively extends the duration of TP-AGB phase. When the conditions are suitable to form carbonaceous dust, the star starts to lose mass consistently as shown in Fig. 4.31b. On the opposite, the case in Fig. 4.31e has not reached this "activation point" before diverging. In order to see the effect of $\dot{M}_{\rm dust}$ on a different model, $\dot{M}_{\rm pulsation}$ has been substituted by $\dot{M}_{\rm B}$. This considerably speeds up the evolution, so we are able to reach a suitable environment for a dust-driven wind. Fig. 4.31d shows again that $\dot{M}_{\rm dust}$ efficiently erodes the star envelop, if favorable conditions are met.

As anticipated, changing how the star loses its mass does not only affect the duration of TP-AGB phase. A different surface enrichment is already hinted in Fig. 4.31. Fig. 4.32 shows the evolution of the 3DUP efficiency and the degree of overlap for every model of the grid.

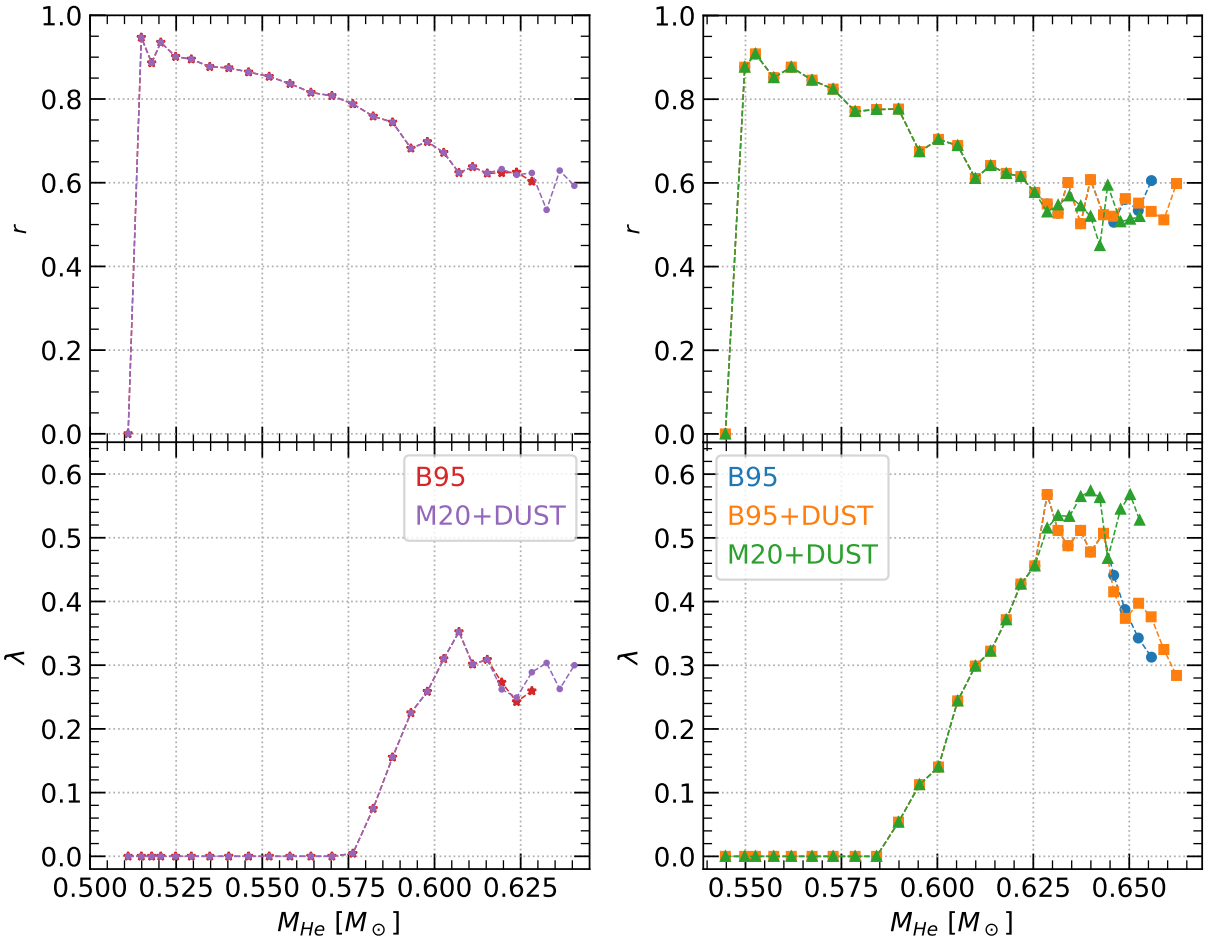

(a) $M_i = 2M_\odot$ **(b)** $M_i = 2.5M_\odot$

Fig. 4.32: λ and r evolution as a function of $M_{\rm He}$ with different mass loss prescription.

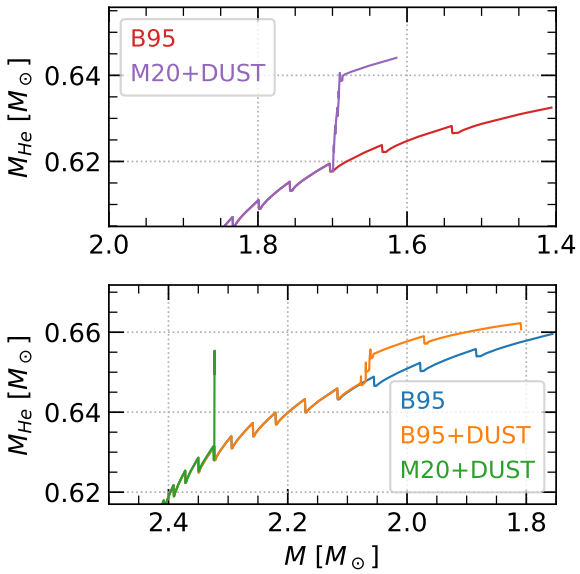

Fig. 4.33: H-free core evolution as a function of the total mass with different mass loss prescriptions. Top panel refers to $2M_\odot$, bottom to $2.5M_\odot$.

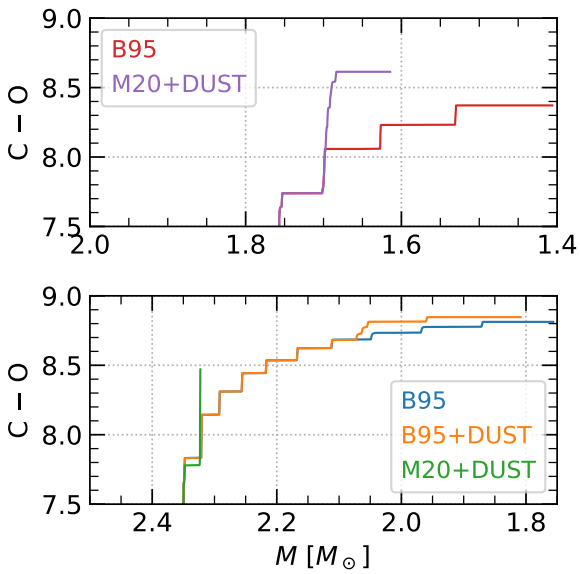

Fig. 4.34: C-O evolution as a function of the total mass with different mass loss prescription. Top panel refers to $2M_\odot$, bottom to $2.5M_\odot$.

We can see that r does not change considerably. The different evolution of the envelope mass instead produce relevant discrepancies on λ. The `M20+DUST` models departs from the others as soon as the prescription is implemented. That is not the case for `B95+DUST`, which follows the `B95` model for the following six TPs. We observe that the overall slower wind (`M20+DUST`) makes λ to stay roughly constant; that is because almost the same envelope mass weigh on the intershell. The case at $M_i = 2.5M_\odot$ shows evidently a considerable drop of 3DUP efficiency. In the end, when the $\dot{M}_{\rm dust}$ activates, `B95+DUST` seems to stay at larger values than `B95`; however additional pulse should be computed in order to confirm the trend. The comparison of the model with $f_{\rm ov,pdcz} = 0.008$ in Fig. 4.12 and `B95` in Fig. 4.32b allows to briefly comments about the numerical resolution. The two tracks are the same ($C = 1$) up to the 18$^{\rm th}$ pulse, then the meshing and timestep parameter is changed to $C = 1/2$ for `B95`. The enhanced resolution results in a larger λ, which is a common behaviour (Herwig et al., 1998). The vast majority of the models presented in this thesis do used $C = 1/2$. Also $C = 1/4$ has been tried, but the extended computing time made difficult to systematically use that resolution. For a quantitative comparison, $C = 1$ models have 2000-2500 mass shells, $C = 1/2$ count 4500-5000 and $C = 1/4$ have roughly 9000.

The λ variation with the mass loss prescription already indicates modifications of the core mass and chemical enrichment. Fig. 4.33 plots the mass of the H-free core for every grid model. The total mass is used as a time proxy; M is a better indicator of how much the TP-AGB phase lasts than the age itself, because the duration of this stage is strongly dependent on the wind prescription. Both panels of Fig. 4.33 highlight how the total mass stays temporarily constant when the pulsation-driven wind sets in. A relevant mass difference builds up between the models with `M20+DUST` and `B95`, affecting the final mass of the white dwarf. The evolution should be continued in order to see the effect quantitatively. The difference is much less pronounced for the `B95+DUST`. That is because also after the RHD routine sets in, sometimes it still produce

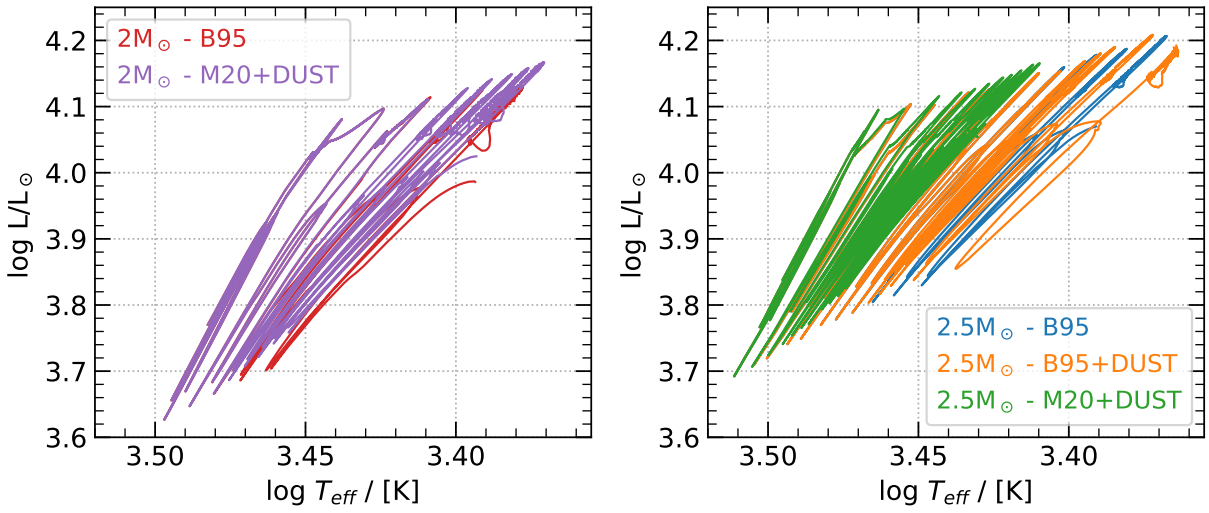

(a) $M_i = 2M_\odot$ **(b)** $M_i = 2.5M_\odot$

Fig. 4.35: Evolutionary tracks with different mass loss prescription. In this figure the track is showed from C/O = 0.85, in order to focus near the point where the mass loss prescription has been changed. The base tracks are collected in Fig. 4.24b.

small or zero $\dot{M}_{\rm dust}$ and `B95` is used. When the "swing" between the two recipes stops, $\dot{M}_{\rm dust}$ has reached values similar to `B95`. Then the evolution keeps going with a smaller discrepancy. A similar picture can be discussed for the chemical enrichment of the surface. That is showed with the carbon excess in the two panels of Fig. 4.34. The models `M20+DUST` potentially build up a larger carbon excess, again because the envelope mass evolution is halted combined with the generally larger values of λ. The other element or isotopic ratios discussed in the previous section go in the same direction. A modification of the chemical enrichment of the surface have crucial consequences in the pollution of the interstellar medium with the ejected material. Fig.

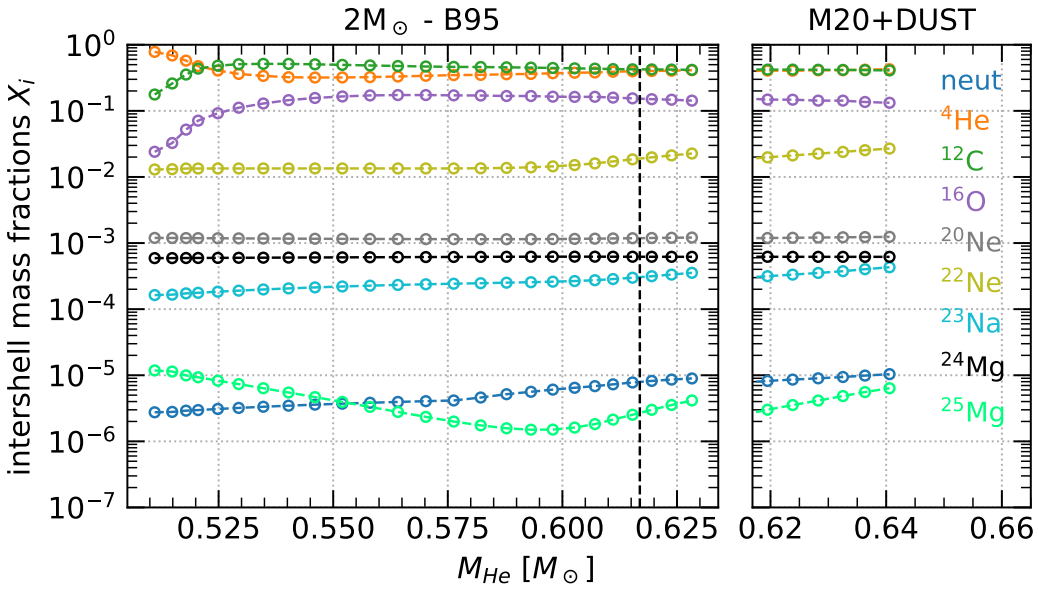

Fig. 4.36: Intershell abundances of 2 $M_\odot$ model with different mass loss prescriptions. The dashed vertical line marks the end of the common part between `B95` and `M20+DUST`.

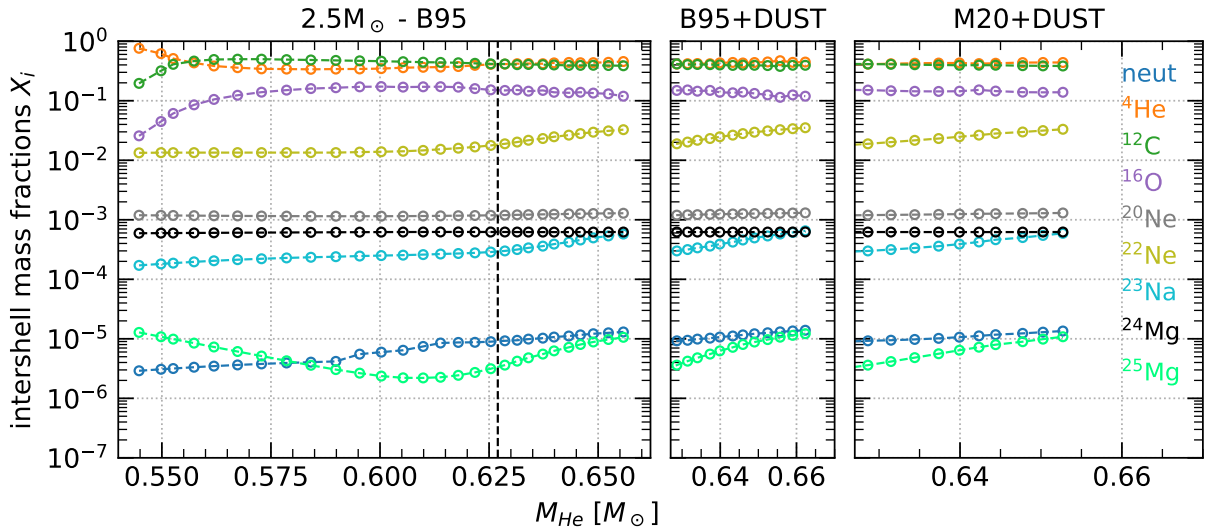

Fig. 4.37: Intershell abundances of 2.5 $M_\odot$ model with different mass loss prescriptions. The dashed vertical line marks the end of the common part among the three recipes.

4.35 shows the coolest and most luminous part of the evolutionary tracks of the grid models. The regions where the track condense in $T_{\rm eff}$ corresponds to period of low mass loss, particularly evident from the `M20+DUST` model at $M_i = 2.5 M_\odot$. On the opposite, the track tend to move to cooler regions for increasing C-O, at least up to saturation (Marigo et al., 2013). We can also observe that the tracks for `M20+DUST` models are found at larger luminosity, which is linked for the systematic increase of the core mass.

The last point I want to discuss is about the intershell composition. We have seen that the degree of overlap is not significantly sensible on the mass loss prescription. That suggests intershell composition should not vary considerably for the models with the same initial mass. Fig.s 4.36 and 4.37 shows the abundances evolution as a function of the $M_{\rm He}$. The points are collected as soon as the pulse driven convective zone is extinguished, but before the third dredge-up takes place. Then it corresponds to the composition of the material mixed with the dredge-up. First of all the plots confirm the expectation; the intershell evolves almost independently on how the envelope loses its mass. However that is not always the case, in the sense that the mass loss still determines when the TP-AGB phase ends. In particular, depending on the mass loss prescription the number of predicted TP changes. Some elements quickly reach their asymptotic value, so that their abundance is almost independent on how the envelope is eroded. Other components are slower, then a different number of TP can build up a difference in the ending chemical composition. That is also the reason why in Fig. 4.23 the abundances for each TP has been plotted.

4.5 Ledoux and Schwarzschild criteria for convection

In this last section I want to briefly discuss about the use of Ledoux and Schwarzschild criteria for convection during the TP-AGB phase. In particular, I will focus on the effects on the efficiency of the third dredge-up, in a more qualitative way. The Ledoux criterion (see Eq. (2.4)) allows to account for composition effects via the mean molecular weight gradients. A

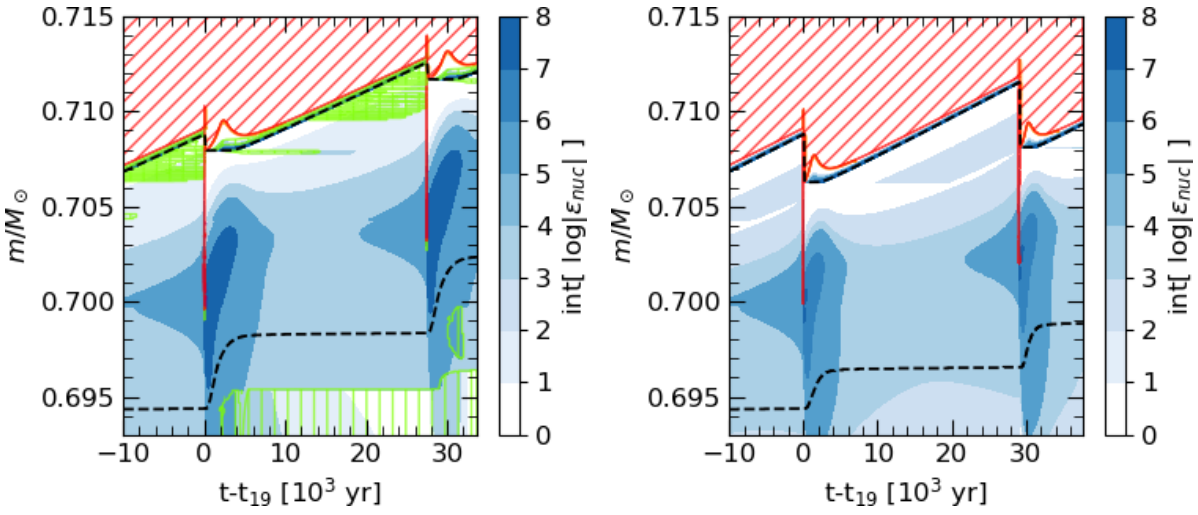

(a) Ledoux criterion.

(b) Schwarzschild criterion.

Fig. 4.38: Kipphenhahn diagram of a $M_i = 3M_\odot$ during 19$^{\text{th}}$ and 20$^{\text{th}}$ pulses. Overshooting is not applied at PDCZ boundaries. Panel (b) has been computed by setting the Schwarzschild criterion at $t - t_{19} = -10$ 10^3yr. The base model is computed with Ledoux recipe, and $t_{19} = 475.7$ Myr.

detailed review on misuses and issues involved in finding the convective boundaries is given by Gabriel et al. (2014). Fig. 4.38 shows the interior structure of a $3M_\odot$ star during a TP cycle computed with the two criteria. It is evident that the third dredge-up takes place, but it is particularly less efficient for the model with Ledoux criterion. We have seen throughout the thesis that λ has critical evolutionary effects. In particular, in this case we expect a lower contamination of the surface chemical composition by the intershell material. That makes much more difficult to produce carbon stars, which are observed. Since the testing case has $M_i = 3M_\odot$, the situation is even worse at lower masses for which λ is typically smaller. A deeper investigation is needed, comparing complete tracks calculated with the two criteria and their final yields and core masses. The test model at $3M_\odot$ was the only one calculated in this thesis, and It also showed a late appearance of the third dredge-up respect to its counterpart using Schwarzschild criterion. For now, It seems that accounting composition effects works against the third dredge-up. Another interesting feature of the models with Ledoux crtierion is that they show the presence of thermohaline mixing also in the TP-AGB phase. However it turns out (Cantiello & Langer, 2010) that in this case the effect on the surface composition is negligible, because of the short timescales of the TP-AGB evolution.

Concluding remarks

The main purpose of this thesis is to analyze in detail the evolutionary effects of the third dredge-up. The structure well reflects how the study has developed. Chapter 2 illustrates the steps taken to get familiar with the `MESA` stellar evolution code and to explore its capabilities, together with the procedure to select the appropriate input physics. Then Chapter 3 discusses the predictions for the first two dredge-up episodes, standard mixing events well known in the literature. Our results are in line with other studies, which supports the performance of the `MESA` models.

The main topic of this thesis, related to the third dredge-up occurring during the TP-AGB phase, is fully addressed in Chapter 4. In particular, we paid particular care to investigate the effects of the mixing treatment applied to the boundaries of the pulse-driven-convective-zone. Allowing additional mixing favors the occurrence of the third dredge-up: the value of the overshooting parameter $f_{\rm ov,pdcz}$ itself mainly affects the relative proportions of the chemical species in the intershell (mostly ^{4}He, ^{12}C, and ^{16}O), rather than the efficiency of the third dredge-up λ. An important comparison is made with the observed abundances of a particular class of hydrogen-deficient post-AGB stars, the so-called PG 1159 stars and the WC central stars of planetary nebulae. Having lost almost all their hydrogenic envelope, the PG 1159 and WC stars are particularly interesting since they are thought to exhibit just the intershell composition left by the last thermal pulse. The comparison clearly indicates a certain amount of convective overshoot is necessary to explain some of the observed abundances, but there are also cases compatible with zero overshoot. The values of the $f_{\rm ov,pdcz}$ parameter suitable to match the observations should vary within a range, typically $0 \lesssim f_{\rm ov,pdcz} \lesssim 0.008$. An extended grid of TP-AGB models with different initial masses has been computed with the calibrated $f_{\rm ov,pdcz}$ parameter.

The final part of the thesis focuses on the effect of mass loss. In addition to the existing options I implemented in the `MESA` code new mass-loss prescriptions of the recent literature. We examined, in particular, the case of radiation-driven winds triggered by the large opacity of the carbonaceous dust that condensates in the extended atmospheres of carbon stars. The intimate relation between the efficiency of the third dredge-up – which is responsible of the surface carbon enrichment – and the efficiency of dust-driven wind is investigated. We found

that not all carbon-rich models are able to activate efficient winds as long as the amount of free carbon (not locked in the CO molecule) is low and does not overcome a minimum threshold. This may have notable impact on the lifetimes of carbon stars and the final mass of their compact remnants, the carbon-oxygen white dwarfs.

In conclusion, we have studied the evolutionary effects related to the third dredge-up of two of the main ingredients of stellar evolution models: mixing treatments and stellar winds. It is well known that the modeling of TP-AGB phase with full stellar models is affected by uncertainties and failures, both of numerical and physical nature. The generation of complete and physically-sound sets of TP-AGB evolutionary tracks is hampered by our deficient knowledge of highly complex processes like those treated here, combined with difficulties related to numerical instabilities and demanding computational efforts. These facts cause a wide heterogeneity across stellar models, which usually bypass the accuracy tests against observations. This work may constitute the ground base of future research, involving the extensive testing and calibration of full AGB stellar models. This preliminary study has been restricted to the `MESA` code, but the effort spent in this thesis may be fruitfully exploited for future developments, that is in the framework of other stellar evolution codes, such as `PARSEC`, and numerical approaches.

References

Angulo, C., Arnould, M., Rayet, M., et al. 1999, Nucl. Phys. A, 656, 3

Asplund, M., Grevesse, N., & Sauval, A. J. 2005, in Astronomical Society of the Pacific Conference Series, Vol. 336, Cosmic Abundances as Records of Stellar Evolution and Nucleosynthesis, ed. I. Barnes, Thomas G. & F. N. Bash, 25

Asplund, M., Grevesse, N., Sauval, A. J., & Scott, P. 2009, ARA&A, 47, 481

Bahcall, J. N., Pinsonneault, M. H., & Wasserburg, G. J. 1995, Reviews of Modern Physics, 67, 781

Bahcall, J. N., Serenelli, A. M., & Basu, S. 2006, ApJS, 165, 400

Basu, S. & Antia, H. M. 2004, ApJ, 606, L85

Bladh, S., Eriksson, K., Marigo, P., Liljegren, S., & Aringer, B. 2019, A&A, 623, A119

Blöcker, T. 1995, A&A, 297, 727

Bressan, A., Marigo, P., Girardi, L., et al. 2012, MNRAS, 427, 127

Bressan, A. G., Chiosi, C., & Bertelli, G. 1981, A&A, 102, 25

Bruzual, A. G. 2007, in IAU Symposium, Vol. 241, Stellar Populations as Building Blocks of Galaxies, ed. A. Vazdekis & R. Peletier, 125–132

Burgers, J. M. 1969, Flow Equations for Composite Gases (New York: Academic)

Cantiello, M. & Langer, N. 2010, A&A, 521, A9

Caughlan, G. R. & Fowler, W. A. 1988, Atomic Data and Nuclear Data Tables, 40, 283

Charbonnel, C. & Lagarde, N. 2010, A&A, 522, A10

Charbonnel, C. & Zahn, J. P. 2007, A&A, 467, L15

Choi, J., Dotter, A., Conroy, C., et al. 2016, ApJ, 823, 102

Chugunov, A. I., Dewitt, H. E., & Yakovlev, D. G. 2007, Phys. Rev. D, 76, 025028

Cranmer, S. R. & Saar, S. H. 2011, ApJ, 741, 54

Cyburt, R. H., Amthor, A. M., Ferguson, R., et al. 2010, ApJS, 189, 240

Dotter, A. 2016, ApJS, 222, 8

Dreizler, S., Werner, K., Jordan, S., & Hagen, H. 1994, A&A, 286, 463

Eriksson, K., Nowotny, W., Höfner, S., Aringer, B., & Wachter, A. 2014, A&A, 566, A95

Ferguson, J. W., Alexander, D. R., Allard, F., et al. 2005, ApJ, 623, 585

Freytag, B., Ludwig, H. G., & Steffen, M. 1996, A&A, 313, 497

Gabriel, M., Noels, A., Montalbán, J., & Miglio, A. 2014, A&A, 569, A63

Hansen, C. J., Kawaler, S. D., & Trimble, V. 2004, Stellar interiors: physical principles, structure, and evolution (Springer-Verlag)

Harper, G. 1996, in Astronomical Society of the Pacific Conference Series, Vol. 109, Cool Stars, Stellar Systems, and the Sun, ed. R. Pallavicini & A. K. Dupree, 481

Henyey, L., Vardya, M. S., & Bodenheimer, P. 1965, ApJ, 142, 841

Herwig, F. 2000, A&A, 360, 952

Herwig, F. 2005, ARA&A, 43, 435

Herwig, F., Schoenberner, D., & Bloecker, T. 1998, A&A, 340, L43

Höfner, S. & Olofsson, H. 2018, A&A Rev., 26, 1

Hu, H., Tout, C. A., Glebbeek, E., & Dupret, M. A. 2011, MNRAS, 418, 195

Iglesias, C. A. & Rogers, F. J. 1993, ApJ, 412, 752

Iglesias, C. A. & Rogers, F. J. 1996, ApJ, 464, 943

Jahn, D., Rauch, T., Reiff, E., et al. 2007, A&A, 462, 281

Kamath, D., Karakas, A. I., & Wood, P. R. 2012, ApJ, 746, 20

Karakas, A. I., Lattanzio, J. C., & Pols, O. R. 2002, PASA, 19, 515

Kippenhahn, R., Ruschenplatt, G., & Thomas, H. C. 1980, A&A, 91, 175

Kippenhahn, R. & Weigert, A. 1990, Stellar Structure and Evolution (Springer-Verlag)

Koesterke, L. & Werner, K. 1998, ApJ, 500, L55

Langer, N., El Eid, M. F., & Fricke, K. J. 1985, A&A, 145, 179

Maeder, A. 2009, Physics, Formation and Evolution of Rotating Stars (Springer-Verlag)

Marigo, P. & Aringer, B. 2009, A&A, 508, 1539

Marigo, P., Bressan, A., Nanni, A., Girardi, L., & Pumo, M. L. 2013, MNRAS, 434, 488

Marigo, P., Cummings, J. D., Curtis, J. L., et al. 2020, Nature Astronomy, 1

Marigo, P., Girardi, L., Weiss, A., & Groenewegen, M. A. T. 1999, A&A, 351, 161

Mattsson, L., Wahlin, R., & Höfner, S. 2010, A&A, 509, A14

Miglio, A., Brogaard, K., Stello, D., et al. 2012, MNRAS, 419, 2077

Paczyński, B. 1970, Acta Astron., 20, 47

Pastorelli, G., Marigo, P., Girardi, L., et al. 2019, MNRAS, 485, 5666

Paxton, B., Bildsten, L., Dotter, A., et al. 2011, ApJS, 192, 3

Paxton, B., Cantiello, M., Arras, P., et al. 2013, ApJS, 208, 4

Paxton, B., Marchant, P., Schwab, J., et al. 2015, ApJS, 220, 15

Paxton, B., Schwab, J., Bauer, E. B., et al. 2018, ApJS, 234, 34

Paxton, B., Smolec, R., Schwab, J., et al. 2019, ApJS, 243, 10

Pignatari, M., Herwig, F., Hirschi, R., et al. 2016, ApJS, 225, 24

Planck Collaboration. 2018, arXiv e-prints, arXiv:1807.06209

Pols, O. R., Tout, C. A., Eggleton, P. P., & Han, Z. 1995, MNRAS, 274, 964

Potekhin, A. Y. & Chabrier, G. 2010, Contributions to Plasma Physics, 50, 82

Reimers, D. 1975, Memoires of the Societe Royale des Sciences de Liege, 8, 369

Rogers, F. J. & Nayfonov, A. 2002, ApJ, 576, 1064

Saumon, D., Chabrier, G., & van Horn, H. M. 1995, ApJS, 99, 713

Slemer, A., Marigo, P., Piatti, D., et al. 2017, MNRAS, 465, 4817

Stanton, L. G. & Murillo, M. S. 2016, Phys. Rev. E, 93, 043203

Thoul, A. A., Bahcall, J. N., & Loeb, A. 1994, ApJ, 421, 828

Timmes, F. X. & Swesty, F. D. 2000, ApJS, 126, 501

Tuchman, Y., Glasner, A., & Barkat, Z. 1983, ApJ, 268, 356

Turcotte, S., Richer, J., Michaud, G., Iglesias, C. A., & Rogers, F. J. 1998, ApJ, 504, 539

Ventura, P., García-Hernández, D. A., Dell'Agli, F., et al. 2016, ApJ, 831, L17

Villaume, A., Conroy, C., & Johnson, B. D. 2015, ApJ, 806, 82

Wagstaff, G., Miller Bertolami, M. M., & Weiss, A. 2020, MNRAS, 493, 4748

Weiss, A. & Ferguson, J. W. 2009, A&A, 508, 1343

Werner, K. & Herwig, F. 2006, PASP, 118, 183

Werner, K. & Rauch, T. 2014, A&A, 569, A99

Werner, K., Rauch, T., & Kruk, J. W. 2005, A&A, 433, 641

Werner, K., Rauch, T., & Kruk, J. W. 2015, A&A, 582, A94

Werner, K., Rauch, T., & Kruk, J. W. 2016, A&A, 593, A104

Willson, L. A. 2000, ARA&A, 38, 573

Zhukovska, S., Dobbs, C., Jenkins, E. B., & Klessen, R. S. 2016, ApJ, 831, 147

Zhukovska, S. & Henning, T. 2013, A&A, 555, A99